Vermindering van de exploratierisico's van gasvelden door innovatieve verwerking van seismische data

Reduction of gas fields exploration risks by innovative processing of seismic data

P. Doulgeris A. Gisolf A. Droujinina
M. Davydenko D.J. Verschuur

Final Report for Project TEUG116268
June 1, 2020

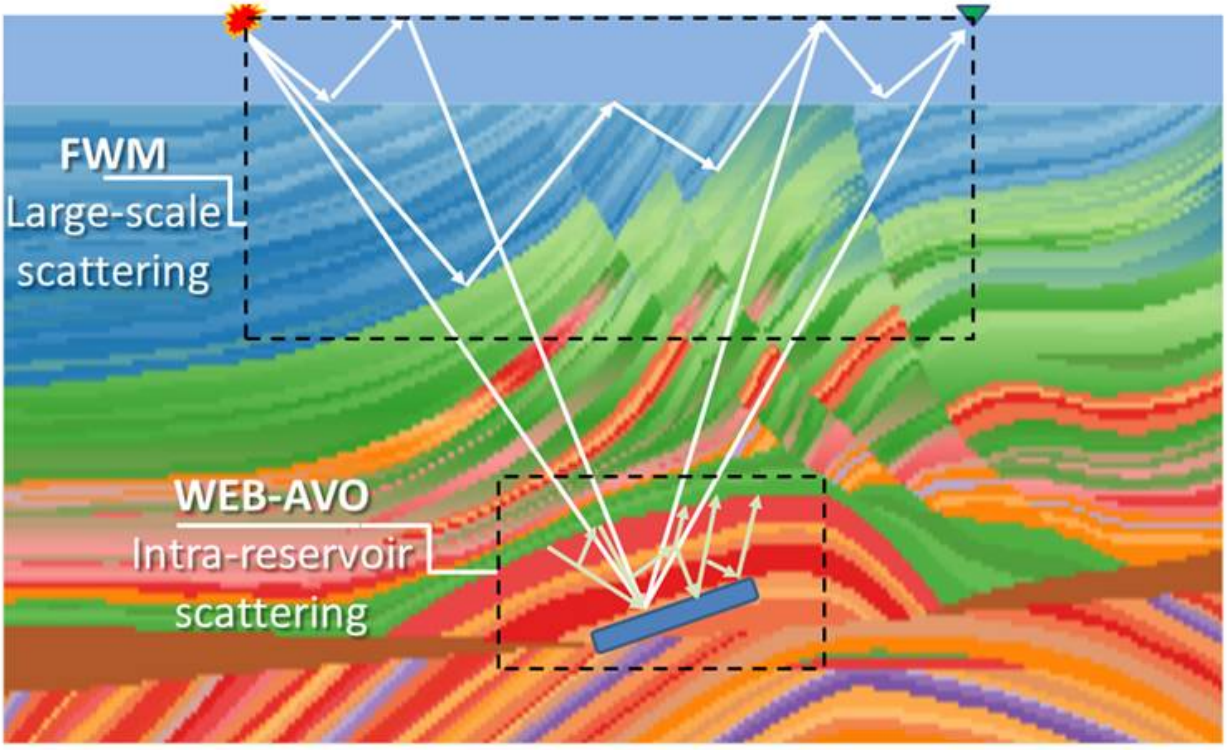

TU Delft Delft University of Technology

DELFT INVERSION

Vermindering van de exploratierisico's van gasvelden door innovatieve verwerking van seismische data

Reduction of gas fields exploration risks by innovative processing of seismic data

by

P. Doulgeris[2] A. Gisolf[2] A. Droujinina[2] M. Davydenko[1]
D.J. Verschuur[1]

Project/Dossier number: TEUG116268
Project duration: February 1, 2017 – January 31, 2019
Involved Parties: ❶ Delft University of Technology,
Faculty of Applied Sciences,
Department of Imaging Physics
❷ Delft Inversion

Final Report, June 1, 2020

This public report is related to Project TEUG116268 that has been executed with a grant from the Ministry of Economic affairs
('Topsector Energiesubsidie van het Ministerie van Economische Zaken')

TU Delft DELFT INVERSION

Contents

1 Introduction

This projects deals with developing innovative approaches to seismic data processing for the quantification of the appraisal of small, proven gas reservoirs in the Dutch North Sea. Over the last tens of years several gas prospects have been discovered in the North Sea. The Dutch part of the North Sea has been extensively mapped with 2D and 3D seismic datasets, which resulted in the discovery of many small and larger gas fields. However, especially for the smaller prospects it is not clear if these are economically viable based on the used seismic processing and imaging techniques. A drawback of the used seismic datasets is that their sampling and subsurface coverage is relatively sparse, making it difficult to extract reliable subsurface information. This means that the uncertainty of the quantification of reservoir potential is too high when it comes to business decisions.

In recent years, processing and imaging technologies have greatly improved. One of the main aspects is that with advanced techniques, the full seismic responses can be utilized in the processing and imaging stage. Due to the fact that seismic waves do not only bounce once in the subsurface, but multiple times, these higher-order bounces in current imaging technologies are neglected and - in addition - provide extra noise in the output. By fully utilizing this higher-order scattering energy, the improvements are two-fold: 1) The 'noise' from these arrivals is removed from the final output, yielding better signal-to-noise ratio and 2) these multiple bounces provide extra illumination, yielding larger coverage of the subsurface area and providing a more accurate description of the reservoir properties.

The aim of this project is to develop a joined work-flow that will bring together two of the most advanced seismic processing and imaging techniques in order to process legacy datasets with the objective of extracting more accurate quantitative information about the gas reservoirs. In addition, improved classification techniques will be developed to further enhance the information extraction from the reservoir in order to reduce the uncertainty and improve the ability to make proper business decisions.

In Figure 1.1 the various Work Packages that were defined in the project are presented. In the next chapters, the results for carrying out each of those work packages are described. Finally, in the last chapter we provide our concluding remarks on the project.

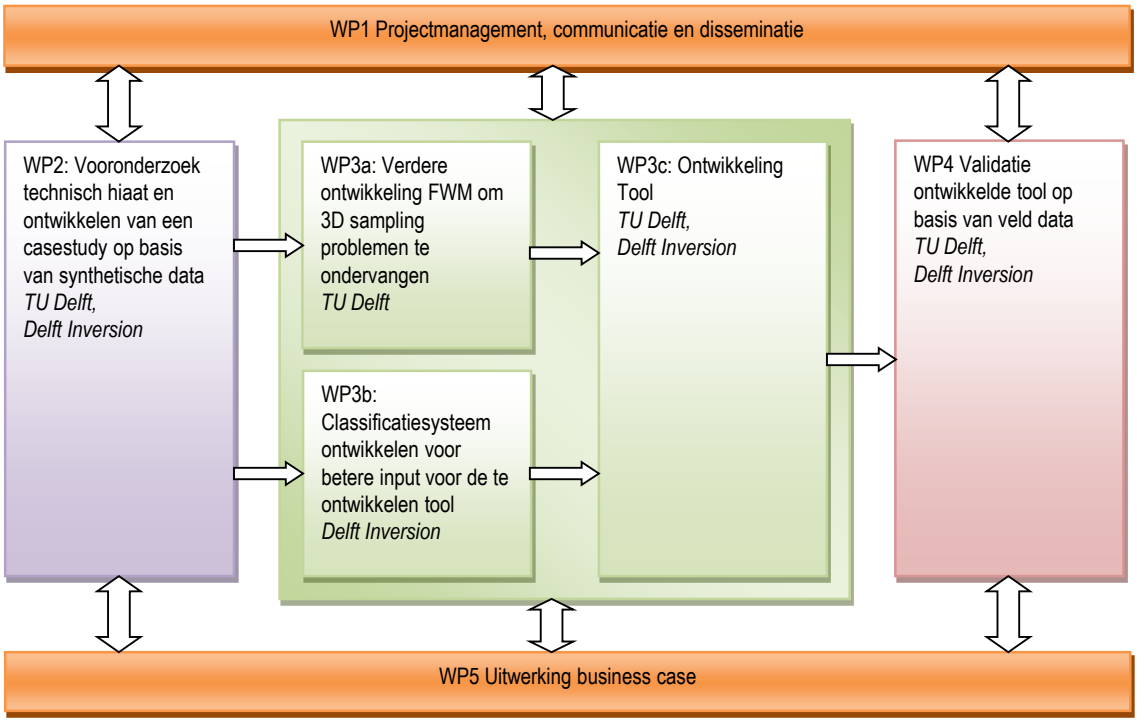

Figure 1.1: Workpackages defined in the project.

2 WP2: Development of a synthetic case study

2.1. Introduction

Work Package 2 deals with the building of a synthetic model that simulates the geology of a gas reservoir in the North Sea. This model will serve as a basis for creating synthetic seismic data that, in turn, will be used as a demonstration dataset for the combined FWM/WEB-AVO work-flow. The complexity of the produced model should be kept at a minimum since the objective is to create a simple-enough, yet representative, dataset in order to check whether all the processes are working as expected. The Dutch sector of the North Sea is known for their complex salt tectonics, with complex Zechstein salt structures van Winden (2015). These salt structures have strong reflectivity (Figure 2.1) and thereby generate strong multiples in the deeper part of the seismic data, where some of the reservoir layers are situated.

Therefore, the synthetic study will concentrate on a situation with a strong multiple-generating overburden overlaying the reservoir are. In the following a 2D analysis of the full wavefield approach is demonstrated as a prior study for the full 3D implementation, that will be reported in Chapter 3, with a synthetic case study of the proposed 3D tool on this synthetic 3D data in Chapter 5.

2.2. 2D synthetic study

To demonstrate the potential of the proposed approach, an initial study on a synthetic 2D case has been carried out. Based on the model shown in Figure 2.2 we created an elastic seismic dataset at the surface. Next, we applied the full wavefield redatuming approach (as will be described in Chapter 3) to arrive at the local impulse responses at the reservoir.

After that, the WEB-AVO technique is applied for the target area indicated by the dashed box in Figure 2.2. In Figure 2.3 a detailed display of the true reservoir properties in terms of three elastic parameters is displayed, together with the background information used in the WEB-AVO inversion (see Chapter 4 for a more thorough description).

The estimated reservoir contrasts (i.e. difference of estimated properties with respect to the background values) are shown in Figure 2.4b, while the true contrasts are displayed in Figure 2.4a. We also compared this to applying the same WEB-AVO approach, but to input data obtained from a standard imaging work flow. These results are displayed in Figure 2.4c.

Note that the proper handling of multiple scattering in the overburden results in a

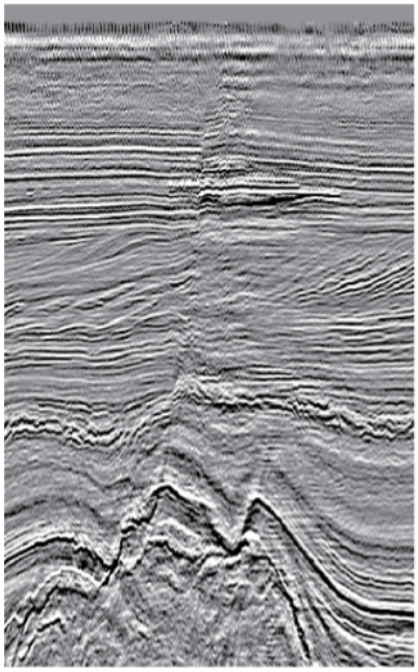

Figure 2.1: A typical seismic section in the southern part of the North Sea, i.e. the Dutch sector, showing the shallow water and the strong Zechstein salt boundary at the bottom (from Silva et al., 2019).

more reliable estimate of the reservoir properties (Figure 2.4b), which, in turn, will provide a more reliable quantification of the assumed producible hydro-carbons. When the overburden is not correctly taken into account, this shows up as a distortion of the estimated contrasts in the reservoir, especially with respect to the shear compliance M (Figure 2.4b), which is an essential parameter for hydro-carbon indication.

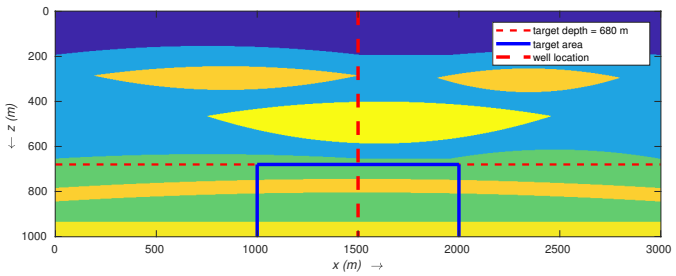

Figure 2.2: Subsurface model for testing the integration of full wavefield redatuming and local elastic inversion (WEB-AVO).

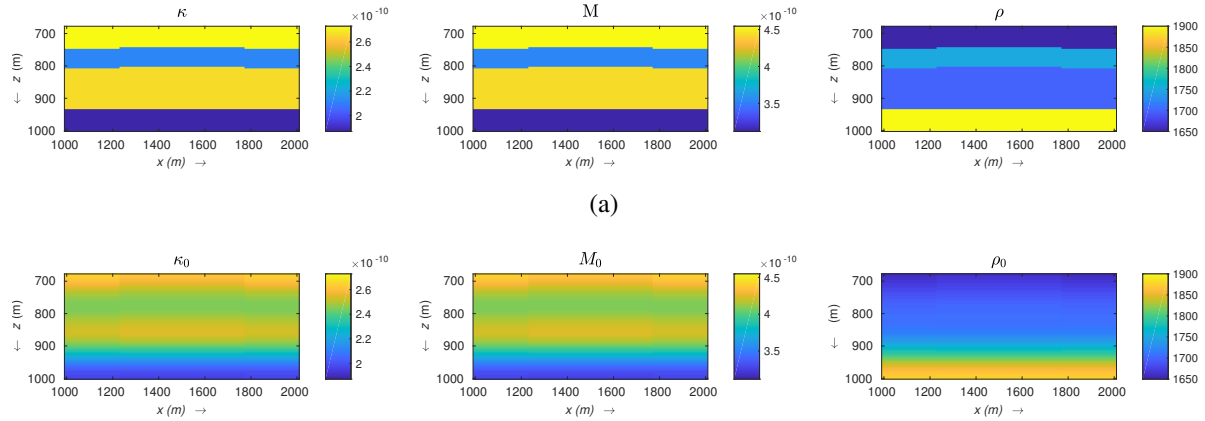

Figure 2.3: a) True and b) background κ (left), M (middle) and ρ (right) in the target domain.

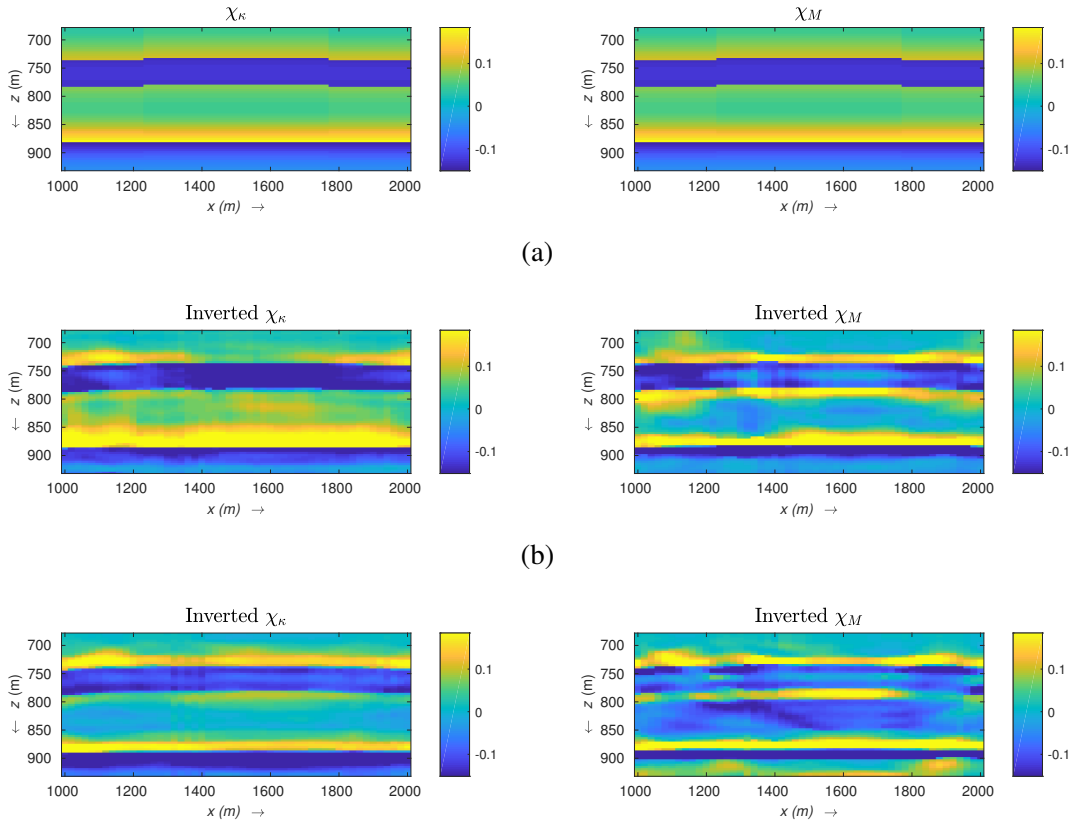

Figure 2.4: True (a) and estimated contrast functions $(\mathrm{X}_\kappa, \mathrm{X}_M)$ b) via the newly developed integrated full wavefield route and c) via the standard redatuming route at all CMP locations in the target domain.

3 WP3a: Reservoir response estimation in 3D using full wavefield migration

3.1. Introduction

Work package 3a contains the advanced imaging algorithm to be applied to the 3D seismic surface data. By using the available, sparse seismic data, we utilize all possible scattering in order to fill in the acquisition gaps, reducing the so-called acquisition footprint, and provide high-quality input for the next step (in Workpackage 3b), which is the reservoir characterization via the WEB-AVO methodology.

3.2. Background of the full wavefield imaging and redatuming methodology

In a high-fidelity workflow for obtaining accurate elastic parameter estimates from the reservoir, first local responses in the linear-Radon domain need to be generated, after which they are used as input for elastic full waveform inversion (Gisolf and van den Berg, 2012). However, estimation of these angle-dependent reservoir responses can be challenging due to various reasons. First, the accuracy of the result depends on the acquisition coverage, which can be insufficient in 3D surveys. Another important factor is the complexity of the medium. A strongly scattering overburden can distort the response from the target area by the inference of overburden multiples with the target reflections. This will happen if for the target response estimation a traditional correlation-type back-propagation process (i.e. redatuming process) is used (see e.g. Berryhill, 1984; Wapenaar and Berkhout, 1989). In this paper the problem is solved by embedding the target response estimation into the Full Wavefield Migration (FWM) process (see e.g. Berkhout, 2014b; Davydenko and Verschuur, 2017). FWM is capable to handle all multiple reflections in a correct manner and, secondly, provides estimated full up/downgoing wavefields at every gridpoint in the subsurface. From these wavefields at target depth the local impulse responses can be calculated (Garg and Verschuur, 2016).

Extension of such procedure for the full 3D case requires handling of the typical sparse sampling that is present in 3D seismic acquisition. However, an appealing feature of FWM is that it can handle multiples even with sparse source coverage configurations, whereas many of the multiple suppression algorithms require dense source and receiver coverage. As a result, an estimated image of the overburden is obtained in combination with a high-resolution target response dataset, such that both of them - after forward modelling- are consistent with the observed surface data. In addition, both image and response data are free of overburden multiple effects. In this paper

the theory of the extended FWM process - including the target response estimation - is presented and an example for 3D modelled finite difference data is shown.

3.3. Method

We consider the **WRW** matrix notation (Berkhout, 1982), which describes the seismic for one frequency component. One vector represents the monochromatic wavefield from one source experiment for all receiver (x,y) locations, organized in one long vector. The FWM forward model is based on the iterative calculation of the downgoing $\vec{P}_i^+(z_n)$ and the upgoing wavefields $\vec{P}_i^-(z_m)$ at every depth level z_m $(0 < m < M)$ related to one source experiment:

$$\begin{aligned}\vec{P}_{i+1}^+(z_m) &= \sum_{0<m<n}[\mathbf{W}(z_m,z_n)\delta\vec{S}_i^+(z_n)] + \mathbf{W}(z_m,z_0)\vec{S}(z_0)\\ \vec{P}_{i+1}^-(z_m) &= \sum_{n<m<M}[\mathbf{W}(z_m,z_n)\delta\vec{S}_i^-(z_n)],\end{aligned} \tag{3.1}$$

where i is the modelling iteration number, $\mathbf{W}(z_m,z_n)$ is a propagation operator defined between the depth levels z_m and z_n and $\delta\vec{S}^{\pm}$ are the secondary sources:

$$\begin{aligned}\delta\vec{S}_i^+(z_m) &= \delta\mathbf{T}^+(z_m)\vec{P}_i^+(z_m) + \mathbf{R}^{\cap}(z_m)\vec{P}_i^-(z_m)\\ \delta\vec{S}_i^-(z_m) &= \delta\mathbf{T}^-(z_m)\vec{P}_i^-(z_m) + \mathbf{R}^{\cup}(z_m)\vec{P}_i^+(z_m),\end{aligned} \tag{3.2}$$

that are responsible for the transmissions (controlled by the $\delta\mathbf{T}$ operators) and reflections (controlled by the $\mathbf{R}$ operators) of the wavefields. The aforementioned procedure is also referred as full wavefield modelling (Berkhout, 2014a). Every new modelling iteration i adds a new order of scattering. Assuming that at $i = 0$ wavefields are zero, $i = 1$ will compute direct downgoing wavefield $P_1^+(z_m)$ and primary reflections $P_1^-(z_m)$. Next, $P_2^{\pm}(z_n)$ will add first-order scattering, $P_3^{\pm}(z_n)$ adds second-order of scattering, etc.

In FWM the following objective function is minimized:

$$J = \sum_{\omega}||\mathbf{P}_{obs} - \sum_{n=0}^{N}\mathbf{W}(z_0,z_n)\delta\mathbf{S}(z_n)||_2^2, \tag{3.3}$$

which describes the L2 norm of the difference between the observed data and the modeled data based on the scattered wavefields, that are again coupled to the subsurface reflectivities, given the background migration velocity model. Thus, the parameters to be updated are the reflectivities in the subsurface (while transmission effects are linked to the reflectivities, see Davydenko and Verschuur, 2017).

However, for estimating the elastic parameters in the target area, local impulse response functions are required. Therefore, we will modify the FWM process such than only the image up to the top of the target level is estimated, while the target area will be estimated in terms of the local impulse response functions in the linear Radon domain. This can be done as FWM produces the up/downgoing wavefields at every depth level, such that the local impulse responses can be coupled with these fields via spatial convolution. The objective function for FWM combined with reservoir response

estimation can be defined as the following minimisation problem:

$$J = \sum_{\omega} ||\mathbf{P}_{obs}(z_0) - \sum_{n=0}^{N-1} \mathbf{W}(z_0, z_n)\delta\mathbf{S}(z_n) - \mathbf{W}(z_0, z_N)\mathbf{L}_{\omega-h}\mathbf{X}_{\tau-p}(z_N)\mathbf{P}^{+}(z_N)||_2^2, \quad (3.4)$$

such that the image $\mathbf{R}$ is estimated at all overburden depth levels $n = 0 \ldots N-1$, and the last term represents the contribution from the local $\tau - p$ target response $\mathbf{X}_{\tau-p}(z_N)$ that is transformed to the space-frequency domain by the $\mathbf{L}_{\omega-h}$ operator and propagated to the surface with the aid of the propagation $\mathbf{W}$ operators. Note that the observed data for all source experiments are combined in matrix $\mathbf{P}_{obs}$.

Previously, in the 2D case, it was shown that estimation of the target responses directly in the $\tau - p$ domain allows avoiding many artifacts caused by imperfect acquisition (Garg and Verschuur, 2016). The results can be also improved by setting sparsity constraints on the estimated responses. It is also important to mention that the estimated responses are further intended to be used for the localized inversion that holds additional assumptions of 1.5D medium in the target area (Gisolf and van den Berg, 2012). Therefore, in the 3D case, a radial symmetry to the $\mathbf{X}_{\tau-p}$ is imposed such that estimation is performed along a single effective slowness direction p_h, rather than along two components (p_x, p_y). This gives a computational advantage because only one-dimensional Radon transform is required at every point of the horizontal 2D surface (depth level). Furthermore, it will make the impact of having sparse data less dominant due to the created redundancy in the target responses (Gisolf et al., 2015).

3.4. Numerical Example

The proposed target response estimation approach is demonstrated on the following numerical example. Figure 3.1a and Figure 3.1b display the velocity and density models of the subsurface. The model contains the overburden part represented by a dipping layer (included in the density model), a water bottom and a target area represented as two thin layers at depth levels 600 and 800m with a channel structure located in between. The data for this example was generated by 3D finite difference acoustic modelling. There were three source lines modeled, where each line contains 13 shot records. The cross-line source spacing is 240m, the in-line source spacing is 80m. Receiver sampling is 20m in both directions. The data were simulated with non-free surface boundary conditions. Hence, it includes only primaries and internal multiples. The source was a Ricker wavelet with a peak frequency of 15 Hz.

First, the data are used for imaging of the full medium. The imaging was performed in two modes – a primary-only least-squares migration (LSM) and FWM that includes multiple scattering and transmission effects. Figure 3.2a and Figure 3.2b show the LSM and FWM images, respectively. It is visible that the latter result has a proper image of the target area because of correctly handled multiple scattering and transmission effects. E.g. note the suppressed crosstalk and improved amplitudes of the target structures.

Next, the extended FWM process was applied, where the imaging was performed only down to the depth level $z = 500m$, which covers the overburden area, such that the target area below $z = 500m$ is fully represented by the local response $\mathbf{X}_{\tau-p}$

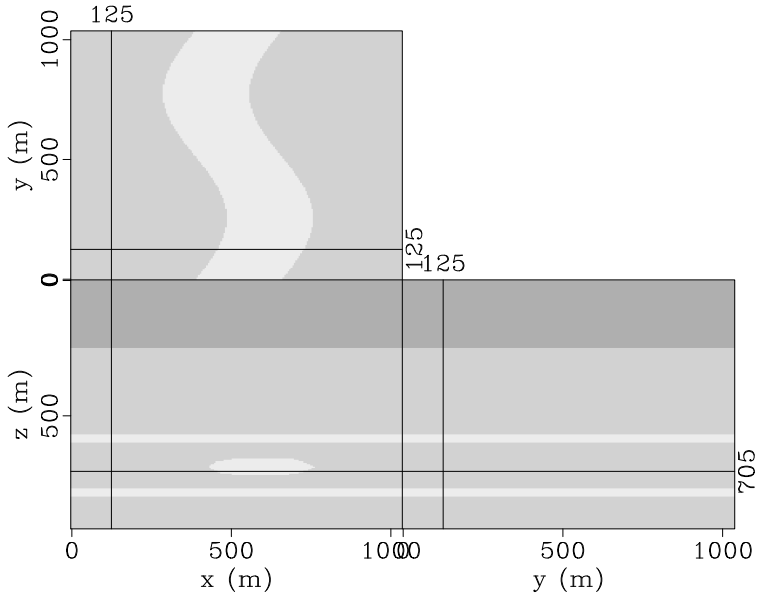

(a) Velocity model

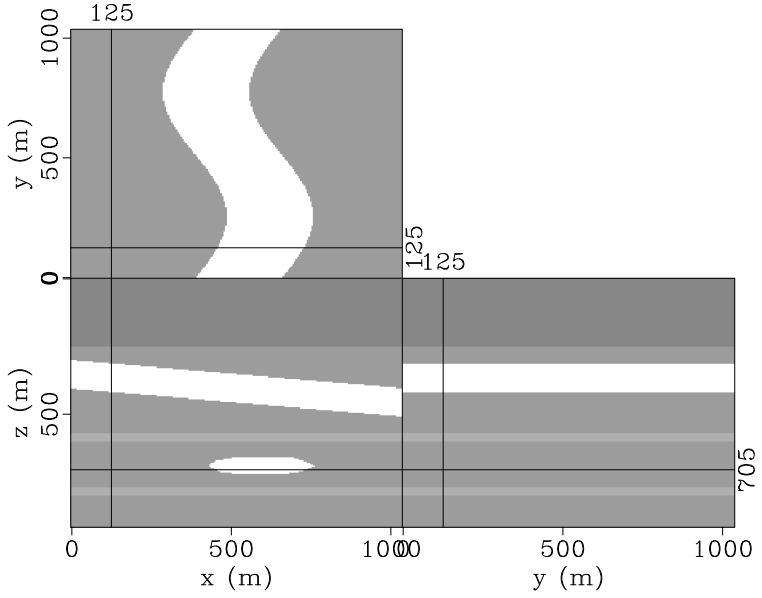

(b) Density model

Figure 3.1: (a) Velocity and (a) density model, where an overburden with a strongly reflecting channel is overlying a reservoir area.

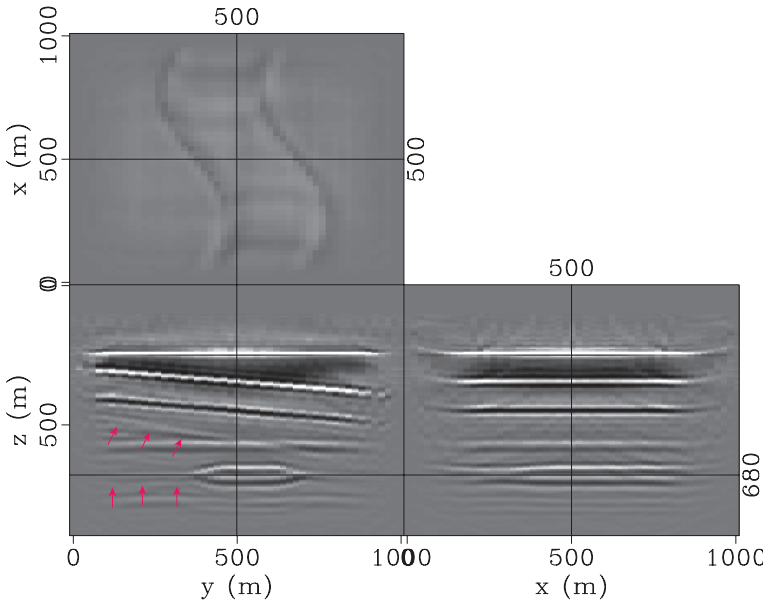

(a) LSM image

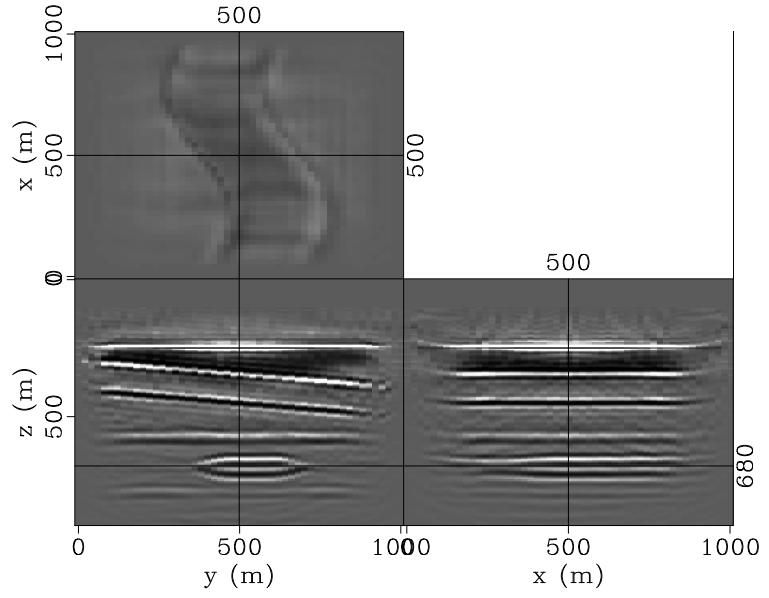

(b) FWM image

Figure 3.2: Complete receivers coverage case: (a) Least-squares migration (LSM) primary-only image and (b) Full wavefield migration (FWM) image. The arrows point at overburden multiples interfering with the target area.

after applying the minimisation problem according to Equation 3.4. Figures 3.3a,b compare a selection (panels) of the responses estimated along a 2D line using LSM-based and FWM-based redatuming, respectively. It is visible that the $\tau - p$ responses obtained using the FWM mode include events with corrected amplitudes compared to the LSM responses. This can be explained by the transmission effects that are correctly included in the forward modelling, which results in the correct amplitude of the downgoing wavefield located at the target depth level. Effect of the overburden interference is also observable: note the extra cross-talk events close to the events associated with the upper horizontal target layer. Also note a better consistency of FWM panels, which is especially visible in the right part of the selected responses. Therefore, from this example it can be concluded that responses obtained by FWM-based redatuming (Equation 3.4 together with Equation 3.1) are more suitable for a further local inversion, such as described in Gisolf and van den Berg (2012).

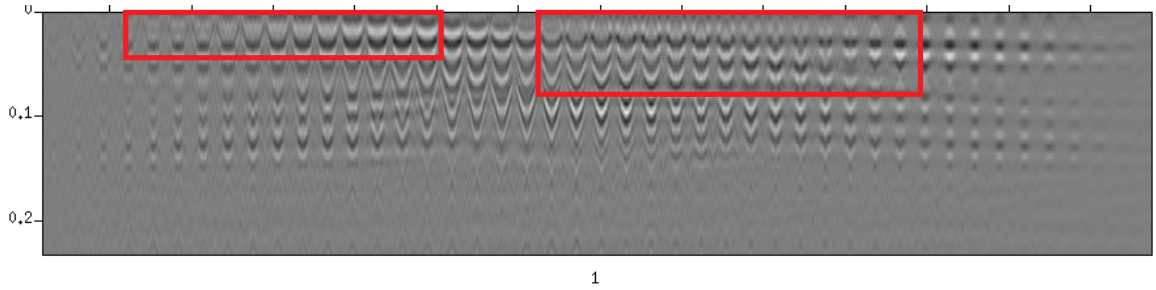

(a) Selection (along a 2D line) of estimated responses based on LSM redatuming

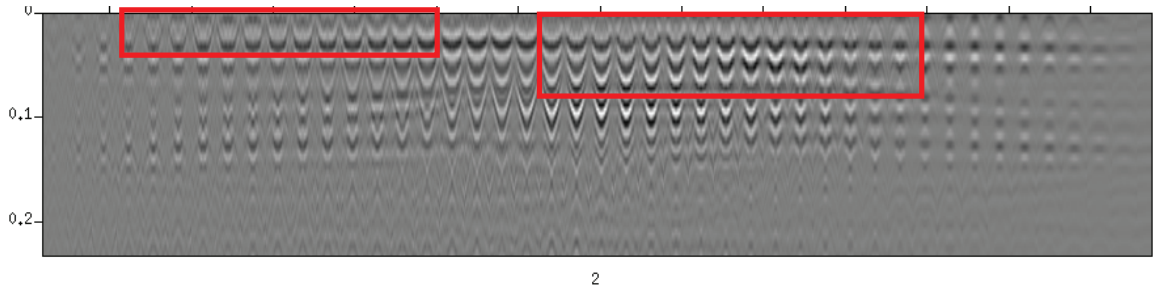

(b) Selection (along a 2D line) of estimated responses based on FWM redatuming

Figure 3.3: Full acquisition case: Estimated local target-layer impulse responses in the linear Radon domain for the case of LSM (a) and FWM (b) redatuming. The boxes indicate areas of multiple interference in the primaries only (LSM) results, which has been resolved by the FWM process.

Finally, we repeat the same experiment but with a reduced amount of the data, in order to create a more realistic narrow-azimuth streamer acquisition scenario: each shot record is limited by in-line offsets starting from 100m, cross-line offsets are limited by the range between -240m and +240m with receiver spacing of 40m (2x decimated). Thus the amount of available data is about 10% compared to the previous case. Figure 3.4 and Figure 3.5 show the estimated images and target responses in LSM and FWM mode. It is visible, that although the imprint of the acquisition becomes observable, the estimation process still provides a robust result and performs correct handling of multiples in the full wavefield case. Note that surface multiples, if included in the estimation process, will remove such acquisition imprint and can provide the required additional illumination.

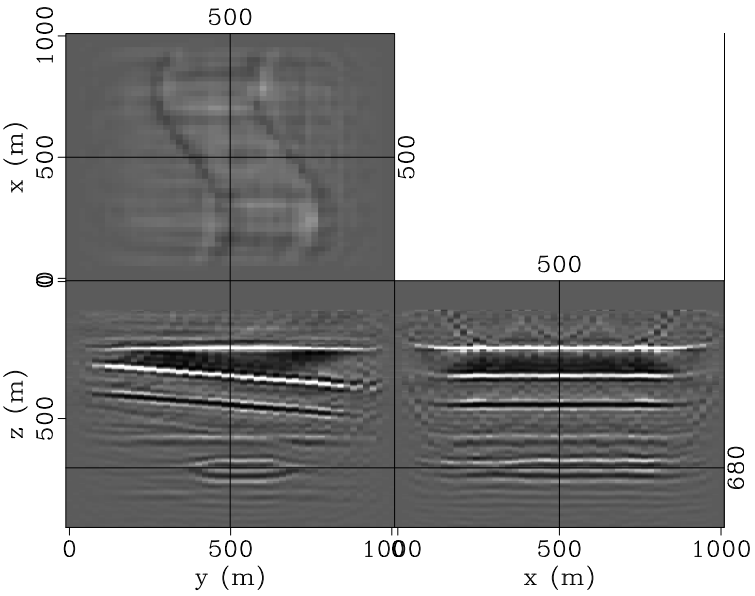

(a) LSM image

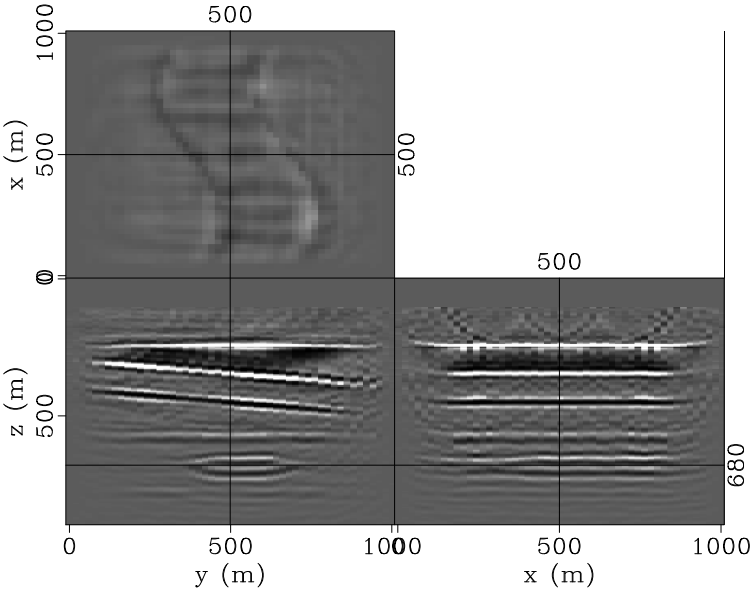

(b) FWM image

Figure 3.4: Narrow azimuth acquisition case: (a) Least-squares migration (LSM) primaries-only image and (b) Full wavefield migration (FWM) image.

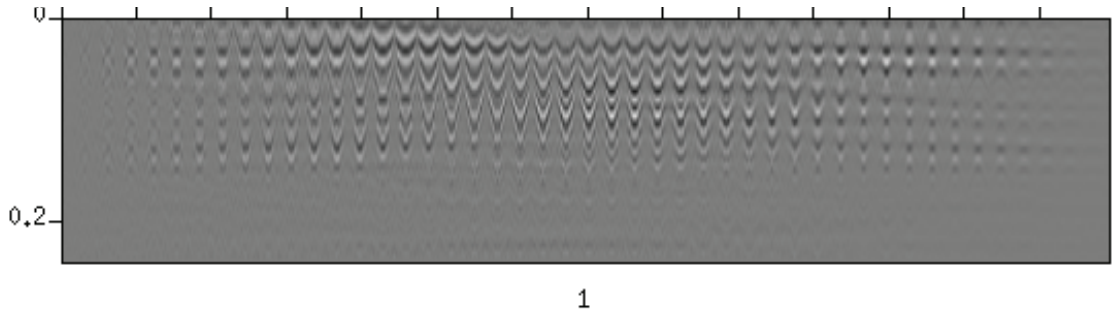

(a) Selection (along a 2D line) of estimated responses based on LSM redatuming

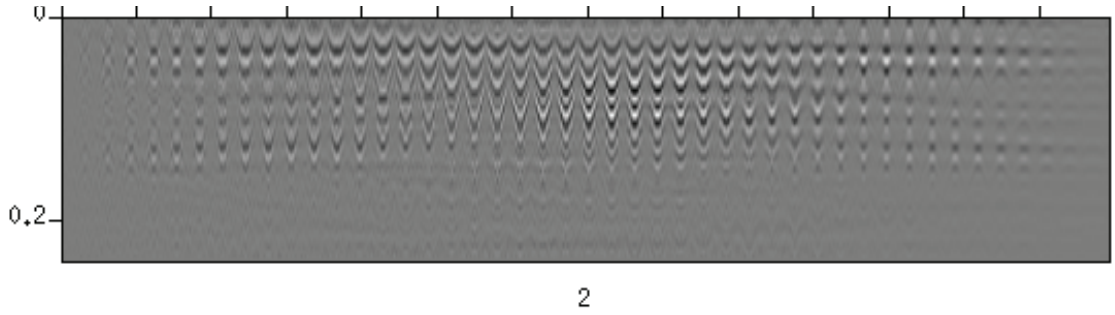

(b) Selection (along a 2D line) of estimated responses based on FWM redatuming

Figure 3.5: Narrow azimuth acquisition case: Estimated local target-layer impulse responses in the linear Radon domain for the case of LSM (a) and FWM (b) redatuming.

3.5. Conclusions on the 3D full wavefield redatuming approach

Correct handling of multiple scattering can be done using full wavefield migration (FWM) – an inversion-based imaging method that includes multiple scattering and transmission effects in the forward model based on the estimated reflectivity. This approach not only suppresses the crosstalk in an automated way, but also allows multiple scattering to actively contribute to the imaging process.

In this chapter it was shown that FWM can be also used in an extended process that combines overburden imaging with the estimation of the local target reflection responses in the 3D subsurface with typically sparse acquisition geometries. Furthermore, the assumption of radial symmetry in the target response releases the redundancy in the data, thus avoiding sparse data artifacts. As both overburden image and target responses are used to explain the observed data, overburden multiple crosstalk is removed and resolution is improved. Correctly estimated target responses are more suitable for the further inversion of the elastic parameters in the target area.

4

WP3b: Development of WEB-AVO and classification system

4.1. Introduction

As part of Work Package 3, Delft Inversion will further develop WEB-AVO for this application while developing a classification system that will be needed for the characterization of gas accumulations in the North Sea. The following paragraphs report on the progress with respect to these two main items.

4.2. Further WEB-AVO development

4.2.1. Introduction to WEB-AVO

In this part of the report we will document a novel methodology developed to preprocess seismic data with the objective of obtaining more reliable elastic parameters (κ and M). Typically, several preprocessing steps are required to produce a suitable input for AVO. First, a background velocity model of the overburden must be estimated through migration-velocity-analysis or full-waveform inversion (FWI). Then, by means of this kinematic model, surface seismic data is localized to the target level through migration and analyzed in the Radon domain (τ-p gathers). Virtual τ-p seismic measurements on top of the reservoir are the input of a typical AVO routine.

The quality of the input data for AVO depends on the kinematic accuracy of the velocity model used for migration. A standard quality-control assessment of this model is based on a measure of 'flatness' of the image gathers (Hinkley et al., 2004; Phillips, 2017; Sigismondi, 2017). However, the criterion of flatness can be deceptive, as it might be affected by multiple scattering and mode conversion. The scope of this study is to analyze the effect of non flatness of the image gather due to incorrect migration velocities on the inverted properties, and design a correction method.

We have observed that an incorrect flattening of the data will produce an apparent misalignment between the inverted properties κ and M, in the sense that the corresponding interfaces (e.g. vertical derivatives) will appear shifted with respect to each other. The fundamental reason must be looked for the uneven contribution of κ and M to the P-wave velocity ($\rho\, c_P^2 = 1/\kappa + 1/(3\,M)$) in many practical scenarios (as the magnitude of M is generally higher than κ).

Mind that a different parameterisation might mitigate or even not produce the misalignment effect. In this sense, the choice for κ and M is convenient, as it offers a measurable criterion—other than flatness of data—for data errors. Clearly, alignment of property structures is the fundamental assumption underlying this work. In the following example, we will illustrate this behavior with the help of a synthetic scenario.

Based on the misalignment mechanism described above, we can then devise a data-correction algorithm that determines a normal-moveout (NMO) correction of the data that optimally removes the misalignment in the property 'domain'. Much can be gained from this correction: not only better aligned properties, but better properties overall from a quantitative perspective, especially when nonlinear inversion is employed. The method is successfully tested on synthetic data.

Throughout this work, we test the correction scheme with the help of a wave-equation based AVO algorithm [WEB-AVO,] (Gisolf et al., 2014), based on an extension of the FWI concept, see e.g., Rizzuti and Gisolf (2017) for a presentation of the main tenets of this approach.

Example

To illustrate the effect of artificial time shifts to the input image gather on the inversion result, we propose the following example. Given synthetic data $d = d(\tau, p)$ in the Radon domain, we apply the following artificial correction, corresponding to classical hyperbolic NMO:

$$d_t(\tau, p) = d(\tau - t \cdot s(p), p), \qquad s(p) = \frac{1 - \sqrt{1 - c_0^2 p^2}}{1 - \sqrt{1 - c_0^2 p_{\max}^2}}. \tag{4.1}$$

Here, c_0 is a fixed velocity, and $p_{\max}$ is the maximum p-value contained in the data. The parameter t governs the maximum time shift (in absolute value). We then investigate how the inverted properties change as a function of t.

It is clear that the data error model depicted by (4.1) is rather simplistic. A simple way to enrich the error space is to select different time windows and define an NMO shift for each portion, similarly to (4.1). This can also be combined with selecting a number of p windows and apply time shifts for each of these windows.

PP synthetic data is generated by modeling elastic waves propagating through the 1.5-D logs depicted in Figure 4.1. We apply time shifts to the migrated image gather,

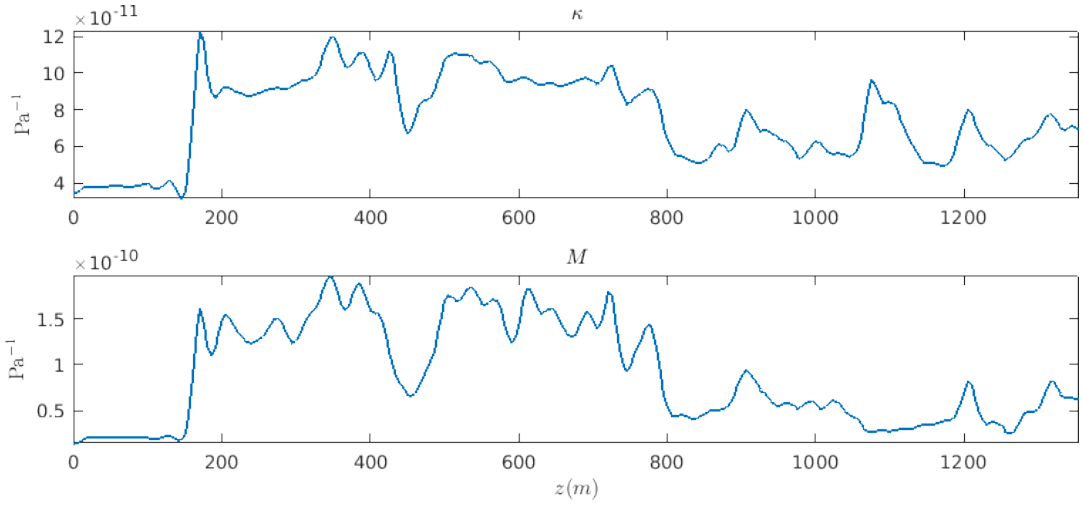

Figure 4.1: Synthetic example model for κ and M, based on true logged properties. The a priori known background model is indicated in red.

following (4.1) (see Figure 4.2).

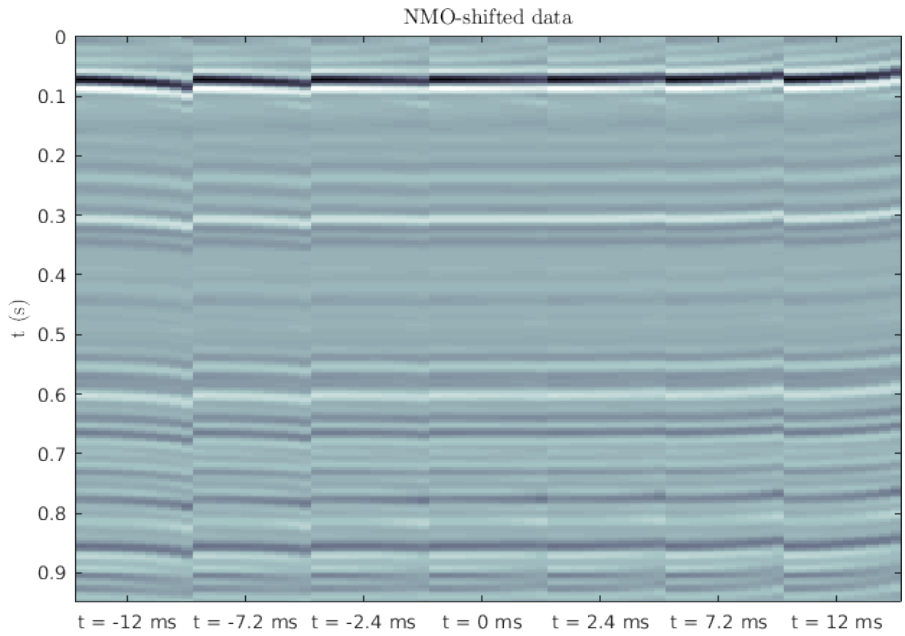

Figure 4.2: Effect of the NMO shift (4.1) applied to the migrated image gather, of which the maximum time shift t ranges from -12 to 12. Each panel is a time-shifted version of the 0 panel.

The results of the AVO inversion are collected in Figure 4.3, where it is shown that the interfaces of κ and M undergo an increasing depth shift with respect to t. However, this occurs at different rates, hence κ and M will appear misaligned with respect to each other for $t \neq 0$.

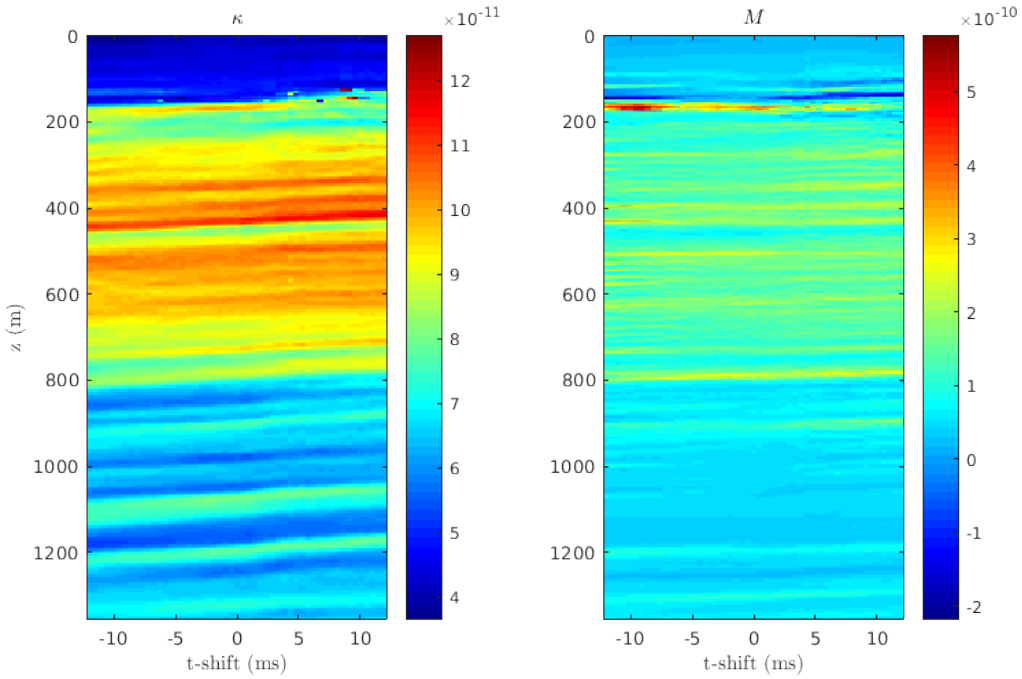

Figure 4.3: Inversion result for NMO-shifted data. Each trace of these pictures represents the inverted property for the corresponding time shift. By comparing κ and M for high absolute values of t, the misalignment will be apparent.

4.2.2. Data correction method

In this section, we setup the optimization framework underlying the data correction based on property misalignment. Note that we assume that the model is locally horizontally homogeneous (the so-called 1.5-D case), as is the case for many AVO schemes. Therefore the problem can be split in many 1-D reconstructions, for which the spatial dependence is on depth only.

The main ingredient to determine misalignment is the cross-correlation of derivatives, defined by

$$(u \star v)(z) = \int_{-\infty}^{+\infty} u(z' + z)v(z')\mathrm{d}z',$$

for two generic functions u, v. An objective functional can then be set which measures the absolute value of the relative misalignment of the derivatives of the inverted κ and M, as a function of the time-shift t. In other words, we define

$$J(t) = \left|\arg\max_z \left|\left(\frac{\mathrm{d}\chi_\kappa^t}{\mathrm{d}z} \star \frac{\mathrm{d}\chi_M^t}{\mathrm{d}z}\right)(z)\right|\right|, \qquad (\chi_\kappa^t, \chi_M^t) = \mathrm{INV}(d_t) \tag{4.2}$$

where χ_κ^t and χ_M^t represent the contrast (with respect to a known background model) of the inverted result for the NMO-corrected data d_t. The short-hand 'INV' stands for any inversion algorithm of choice.

Each evaluation of J in (4.2) requires, in principle, running a (nonlinear) inversion INV with data d_t. We simplify the complexity of this step by adopting a linearized version of INV. This is then tantamount to solving a (dense) linear system, whose inverse can be calculated once and stored for multiple usage. Note that the feasibility of this step is due to the 1-D nature of the problem.

The objective (4.2) is a real-valued function of a single variable and we can resort to derivative-free optimization algorithms such as the Nelder-Mead method Nocedal and Wright (2006). For the very simplistic case of the data error model here considered, we can even directly sample the t-space and 'manually' pick the minimum. Note that the objective might be riddled by singular points. We assume that the data error is not so significant that such problem will occur.

When a more sophisticated data error is chosen, with respect to the simple model (4.1), the dimension of the error space should be limited in order to keep the problem well posed and be able to employ derivative-free methods, whose performance degrades rapidly with dimension. In this paper, we will stay with (4.1).

Example

We test the correction scheme described in the previous section. For each time shift, the inversion algorithm is run with the corresponding corrected data. The result is summarized in Figure 4.4, which demonstrates the effectiveness of the method. The properties are now flat across the time shift variable t, contrary to Figure 4.3. The method is successful in recovering the correct time-shifts t that were used to artificially perturb the data.

4.2.3. Summary and conclusions

In this work, we studied the effect of incorrect NMO shifts applied to flatten the data, which can affect AVO inversion. Using flatness of data as the sole criterion for data

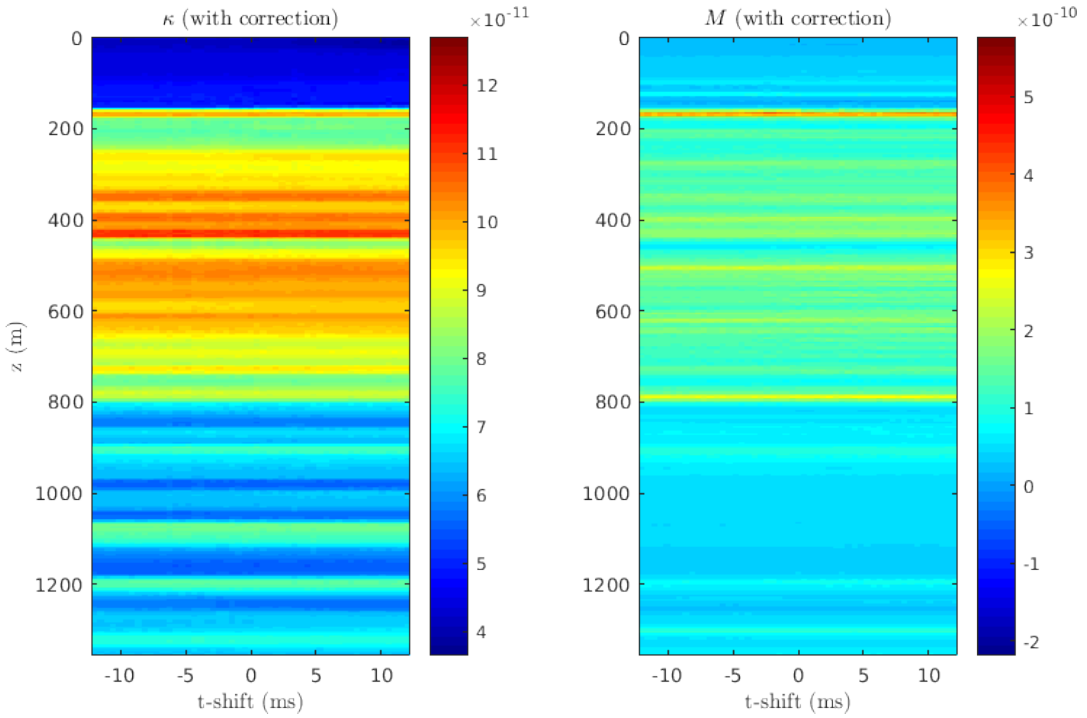

Figure 4.4: Inversion result for NMO-shifted data in combination with the data correction scheme. Compared to Figure 4.3, the interfaces of κ and M are well aligned.

quality might however be problematic, due to multiple scattering and mode conversion. The main finding, here, is that these kind of errors show up as misalignment in the inverted properties κ and M. Therefore, we devised a correction scheme for the data based on the minimization of such misalignment. We demonstrate these concepts by means of a simplified synthetic scenario.

Much work is needed to extend the method to more realistic data errors and test well-posedness of the problem and convergence of the scheme on a bigger parameter space, hence this is still work on progress.

4.3. Development of a Classification system

4.3.1. Introduction

In order to be able to identify a gas saturated reservoir, a classification system is required. Such a system is trained on available well data from the region and it applies the different classes defined therein laterally over the extent of the area of interest. We will here briefly document the development of this module and the resulting software interface obtained.

4.3.2. Method

The sole purpose of a classification system is to identify to which category an object belongs to. In our case, by object we refer to the voxels obtained by the inversion scheme that have one, two or three parameters (κ, M and ρ) to characterise them. There are numerous methods proposed over the last few decades to perform this

task, see Arabie et al. (1996) for a review, but it is also worth noticing that this field was the basis of more modern fields of mathematics like artificial intellingence and deep learning.

In the context of this project, a classification system will convert the output of WEB-AVO (elastic parameters) to lithofacies, as these have been defined at the well location. The undelying geological assumption is that whatever appears geologically in a vertical sense, appears also in a lateral sense. The only consideration that needs to be made is the compression at different depth levels. In order to mitigate this, depth trends are taken as input to the classification algorithm to correct for possible compaction effects. The classification algorithm chosen to perform the task, is a Naive Bayes Classifier, see Russell and Norvig (1995).

Naive Bayes refers to a family of algorithms that is used for constructing classifiers. All Naive Bayes algorithms are based on the assumption that the value of a particular feature, elastic parameter in our case, is independent of the value of any other feature, given the class variable. For example, a fruit may be considered to be an apple if it is red, round, and about 10 cm in diameter. A naive Bayes classifier considers each of these features to contribute independently to the probability that this fruit is an apple, regardless of any possible correlations between the color, roundness, and diameter features. This is very important aspect that makes this family of algorithms particularly suitable for classifying the output of WEB-AVO, as the parameters WEB-AVO solves for are almost orthogonal to each other, hence they are more independent measurements.

Despite their naive design and apparently oversimplified assumptions, naive Bayes classifiers have worked quite well in many complex real-world situations. An advantage of naive Bayes is that it only requires a small number of training data to estimate the parameters necessary for classification. This is extremely important in the lithofacies classification where only few samples of every lithology may have been encountered in the training set (well logs).

4.3.3. Implementation

A Gaussian Naive Bayes implementation has been chosen for our classifier, i.e. the likelihood of the features is assumed to be Gaussian. This is chosen because Gaussian probabiliby density functions typically work well in geophysical applications. The following equation gives the likelihood function:

$$P(x_i|y) = \frac{1}{\sqrt{2\pi\sigma_y^2}} exp(-\frac{(x_i - \mu_y)^2}{2\sigma_y^2}). \tag{4.3}$$

The algorithm has been implemented using Python and the scikit-learn modules and a simple user interface has been produced, see figure 4.5. The user can define the lithofacies in a visual way, while importing the required depth trends as .dil files (proprietary file format of Delft Inversion) and the elastic parameters as Seismic Unix files.

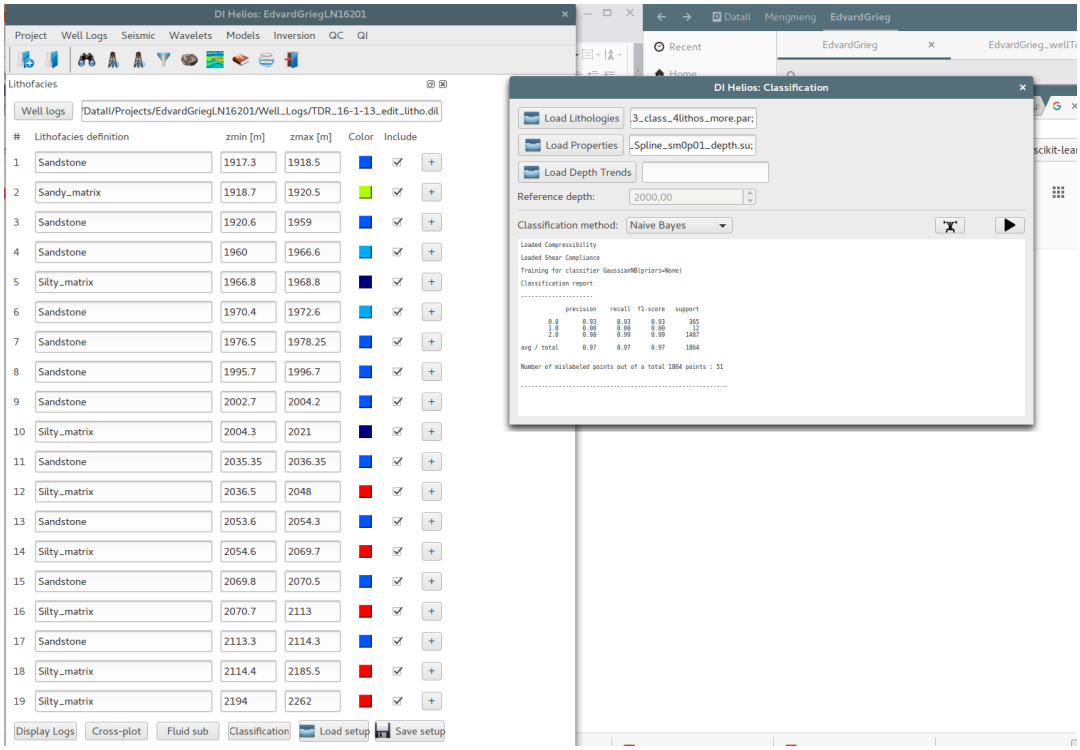

Figure 4.5: Interface for running the Naive Bayes module on the produced elastic parameters. On the left, the user can input the labels of the different classes, whereas on the dialog on the right, they can perform a training and classification of the volumes.

4.3.4. Classification Testing

The classification system has been fully developed and tested on field data. It has been successful in producing robust lithological volumes in cases of accurate seismic-to-well ties. Figure 4.6 shows the results obtained in a field in Norwegian Continental Shelf. In the test case we studied, the tie of the seismic and the well information was poor, hence, this renders any classification attempt meaningless as the obtained results are not calibrated at the well locations.

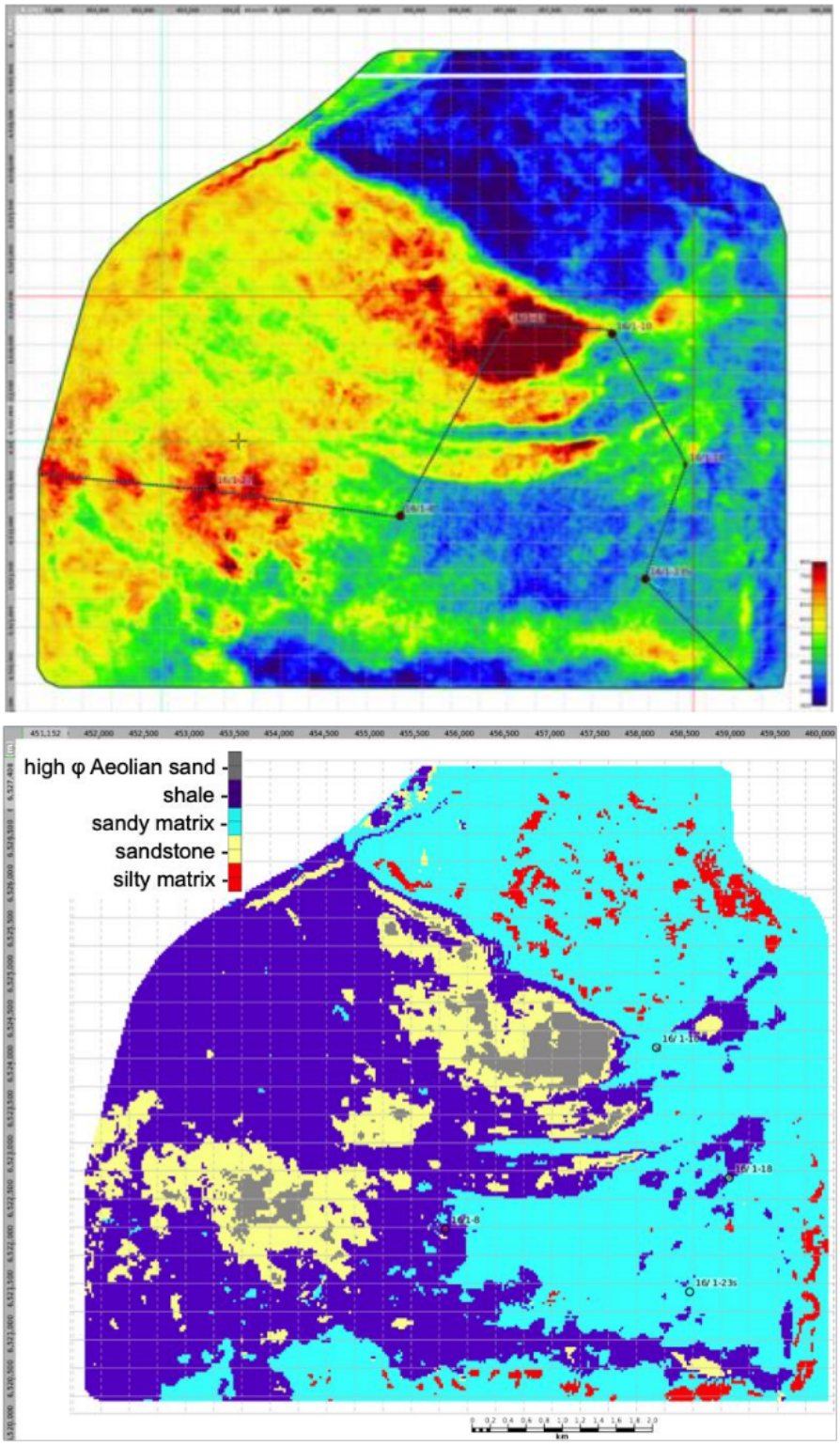

Figure 4.6: (top) Compressibility volume derived from seismic gathers in a field in Norwegian Continental Shelf. (bottom) Lithology volume calculated with the classification system developed.

5

WP3c: Integration of partial techniques

The last step in Work package 3 is the integration of the two main tools, begin the full wavefield redatuming (WP3a) and the WEB-AVO process (including the classification, WP3b) into one final tool that allows application to realistic data.

5.1. Full wavefield redatuming on the 3D synthetic data

We used the synthetic example shown in Chapter 3 as a test case, because it contains a strongly reflecting overburden, which generates noticeable internal multiples in the target area. This is similar to the case in the North Sea where strong salt body reflections, together with other overburden reflectors, create internal multiples in the reservoir area. With the full wavefield approach two aspects are taken into account to improve the creation of reservoir-area impulse responses that will be used for the reservoir inversion (WEB-AVO, see the previous chapter): 1) The inversion approach followed will take the maximum advantage of all downgoing wavefields – primaries and multiples – to contribute to a good illumination of the target area and 2) the full wavefield approach will correct for overburden transmission effects and internal multiples, such that an equalized and overburden multiple-free target response can be obtained.

Figure 5.1 shows the first step in this process, being the full wavefield redatuming, creating a local angle-dependent impulse response at the datum level of z=500m in the 3D subsurface model (see Figure 3.1). As input we have used only 3 sail lines with a coarse sampling in sources (160 m in-line and 240 m cross-line). By assuming azimuthal invariance of the reflectivity, the redatuming is done by using the local Radon panels - as shown in Figure 5.1 - as the unknowns. However, the inversion-type redatuming was carried out in the primaries-only situation (top of Figure 5.1) and the full wavefield mode (Figure 5.1). Note the interfering overburden multiples in the primaries-only case, while these have been suppressed in the full wavefield case.

A similar observation is made when displaying the zero ray parameter section along the complete middle inline location, shown in Figure **??**, both for the primaries-only (top) and full-wavefield mode (bottom). For the latter case, the channel structure can be well recognized in the redatumed data. Note that this can be considered as pre-stack data at the datum level, although using the local CMP approach, the information for each Radon panel is assumed to belong to a local 1.5D medium, such as used in the WEB-AVO approach.

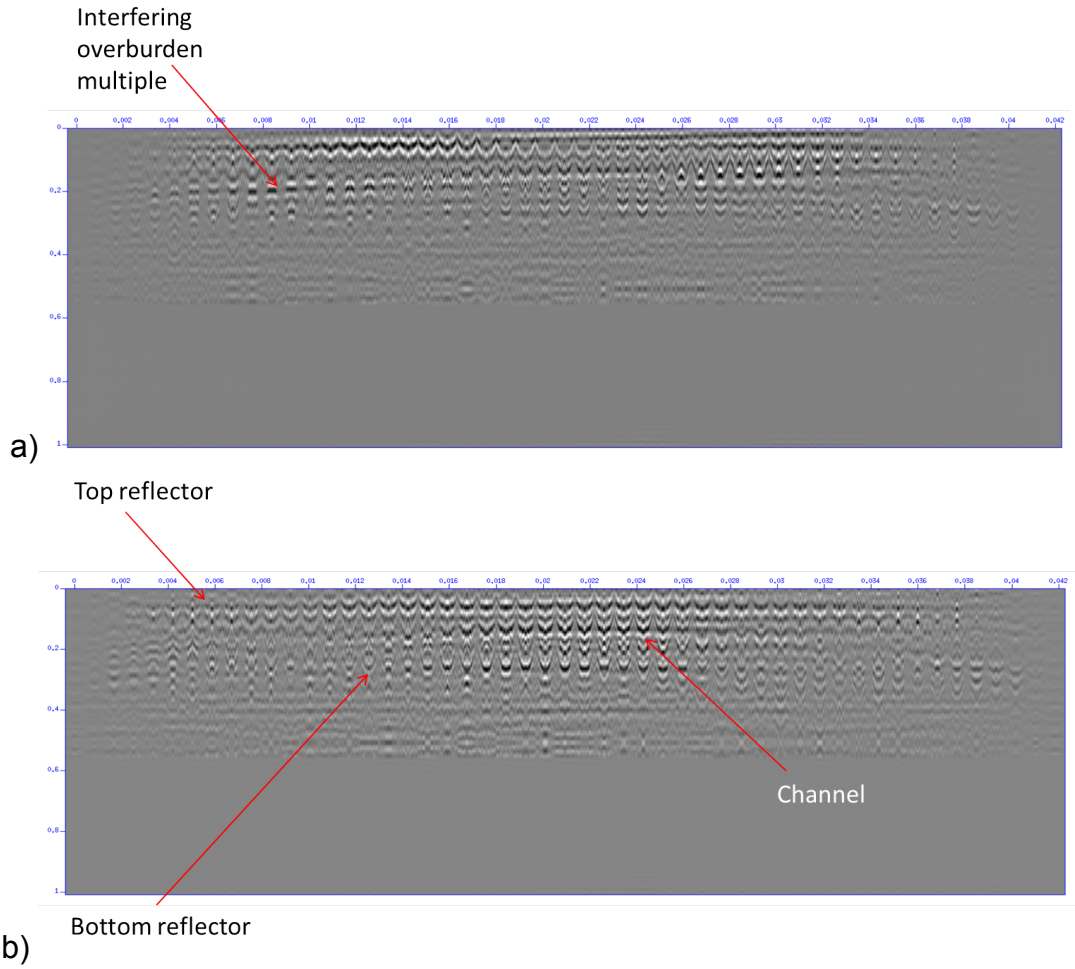

Figure 5.1: A selection of fully redatumed Radon-domain gathers selected along the middle inline after the least-squares redatuming (top) and the full wavefield redatuming (bottom).

5.2. WEB-AVO inversion of the redatumed Radon gathers

Next, these panels are used in the WEB-AVO inversion process, that considers again a full waveform approach, but assuming that the medium starts at the datum level. Therefore, it is crucial that all overburden effects have been removed from these panels.

First, the middle location of the model is assumed to contain the well-log. The vertical cross-section of the model at this location is shown in Figure 5.3, the left side. Note that the model is acoustic, but can still be inverted with elastic WEB-AVO by setting v_s to zero. Next, in Figure 5.3, the Radon panel for the forward modeled reservoir response is compared with the FWM and primaries-only (LSM) redatuming result. It is clear that both redatuming result are not directly resembling the forward modeled response, but the FWM has the largest resemblance. This observation is supported by the comparison in Figure 5.4 in which the small-ray parameter plots are displayed for the modeled responses (top row), FWM result (middle row) and the LSM result (bottom row). Overall, the FWM result shows a much better correspondence to the true

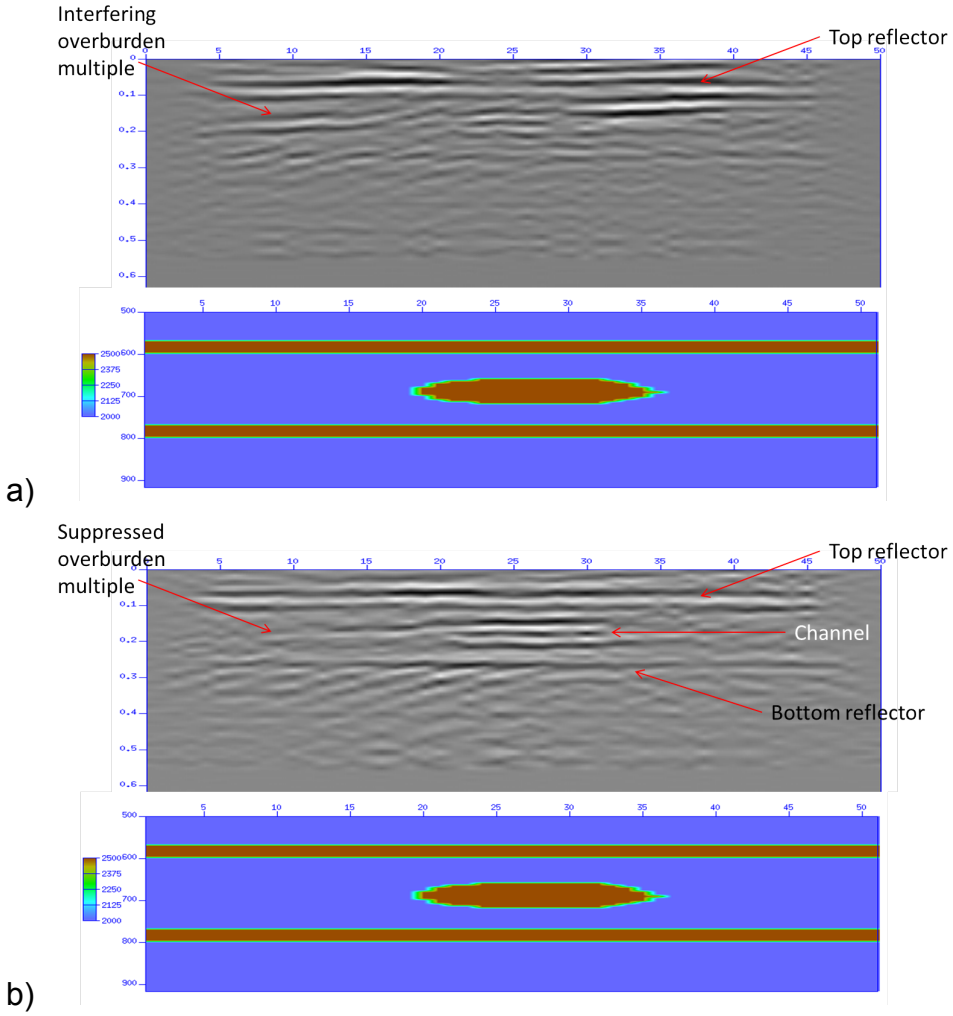

Figure 5.2: The zero-ray parameter panels for the middle inline after the least-squares redatuming (top) and the full wavefield redatuming (bottom).

channel structure, while the LSM result has strong artifacts from residual overburden multiples and transmission effects.

As a second step in the approach discussion this report, the WEB-AVO is applied to all Radon panels. As a background the smoothed version of the true model is used in order to avoid a possible imprint from the choice of background (although WEB-AVO is known to be quite robust for the chosen background). First, the reference results - WEB-AVO inversion applied to the forward modeled responses in the reservoir area - are displayed in Figure 5.6. As expected, the output is accurate in the left and right side, but the contrasts in the channel area are so large – especially for the density – that the WEB-AVO has some issues finding the right contrast parameters. This extreme models pushes the limits for the WEB-AVO process.

If we now use the input from the primaries-only redatuming (LSM) Figure 5.7 is obtained. The results for κ are still quite reasonable for the top part of the model, but in the bottom of the model things are confused due to the residual overburden imprint in the data.

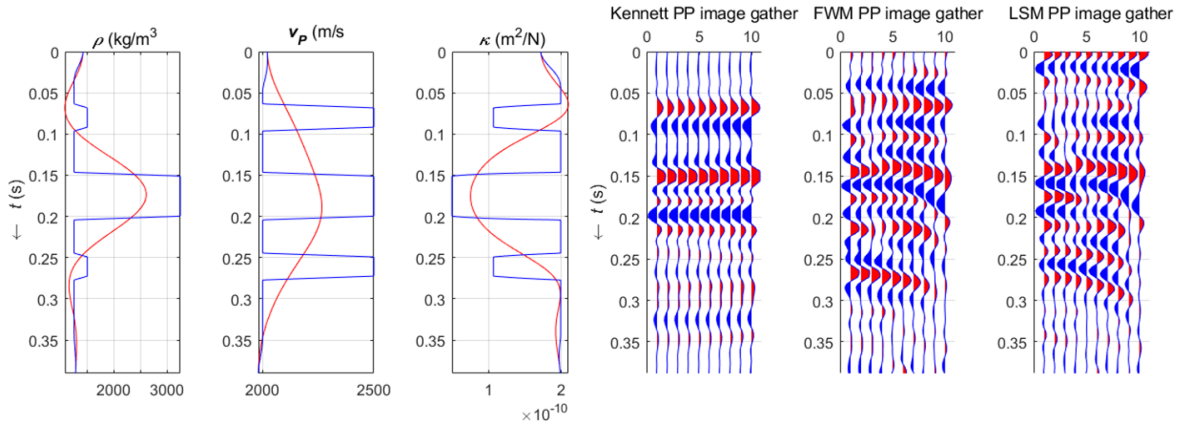

Figure 5.3: Left) The true model at the middle location, displayed as a well-log for ρ, v_p and κ. Note that this is an acoustic model, such that $v_s = 0$. Right) The forward modeled Radon panel, the obtained Radon panels after full wavefield redatuming and the primaries-only result.

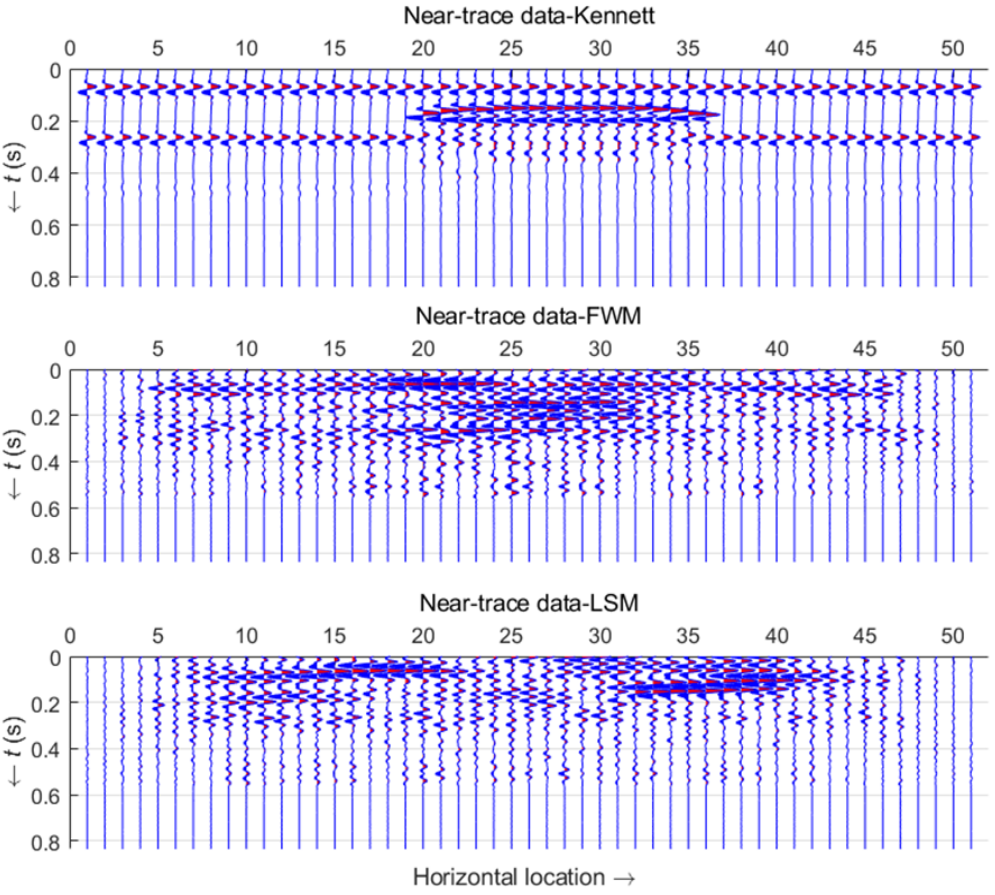

Figure 5.4: Zero ray-parameter gathers along the middle inline (a) directly modeled from the true reservoir model, (b) extracted from the results after full wavefield redatuming and (c) extracted from the result after least-squares, primaries-only redatuming.

Figure 5.8, finally, shows the result of WEB-AVO inversion applied to the FWM panels. The results have clearly improved compared to the LSM result, especially in the lower part of the model. The reflector below the channel has been retrieved to some extend, even below the channel itself.

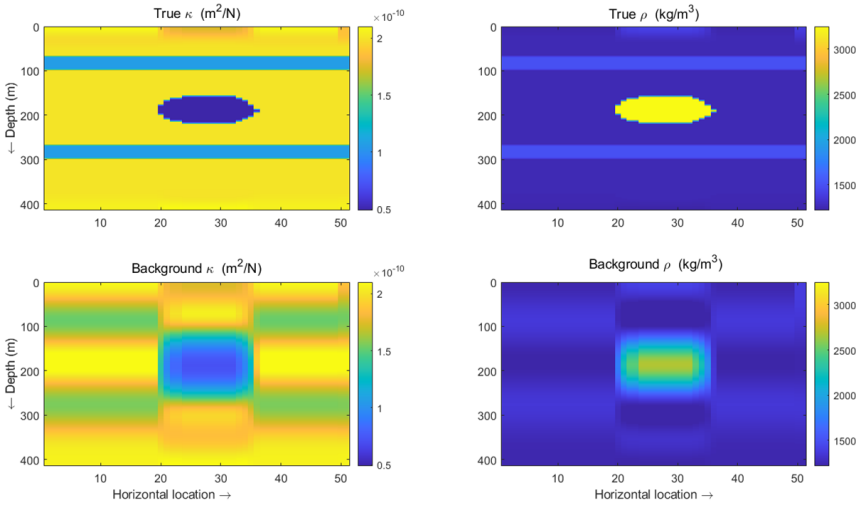

Figure 5.5: The true model along the middle inline (top row) and the smoothed version used as background for the WEB-AVO inversion (bottom row).

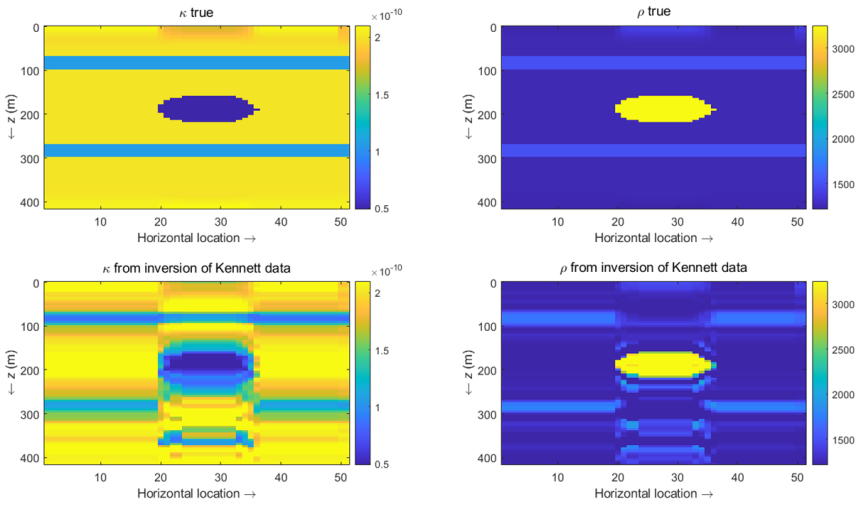

Figure 5.6: WEB-AVO inversion results for the responses forward modeled from the true model. Top row) True model parameters. Bottom row) Inverted elastic parameters κ and ρ.

Also the channel structure is much better defined in the inversion result for κ. Also the 'instable' behaviour in the output for the area around horizontal location nr. 35 in the LSM results have been restored completely by the full wavefield approach.

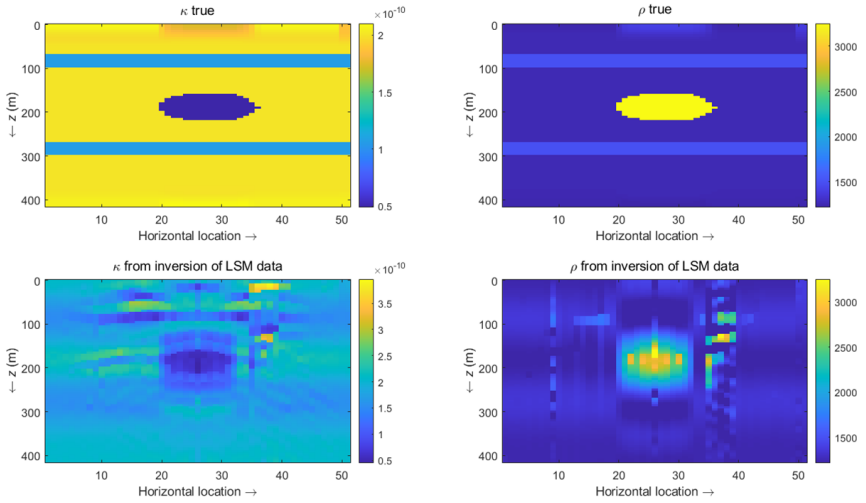

Figure 5.7: WEB-AVO inversion results for the responses obtained after primaries-only inversion-based redatuming, i.e. the panels as shown in Figure 5.1a. Top row) True model parameters. Bottom row) Inverted elastic parameters κ and ρ.

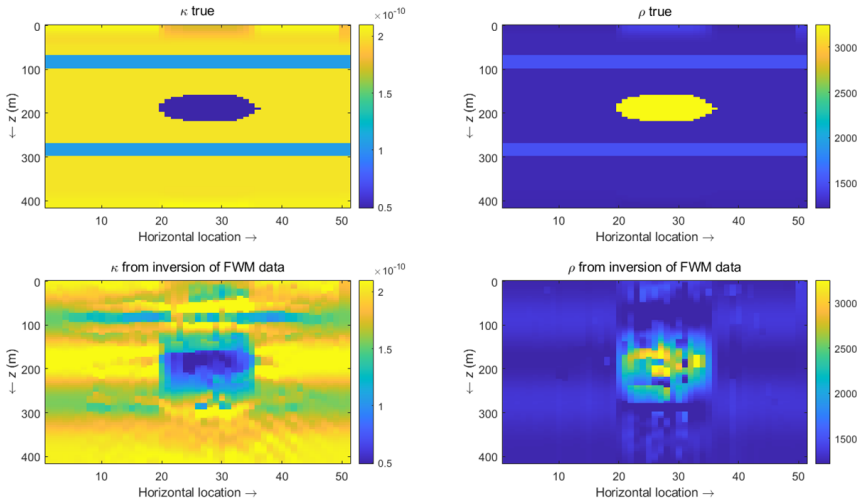

Figure 5.8: WEB-AVO inversion results for the responses obtained after full-wavefield redatuming, i.e. the panels as shown in Figure 5.1b. Top row) True model parameters. Bottom row) Inverted elastic parameters κ and ρ.

6
WP4: Validation on field data

6.1. Introduction

This project deals with developing innovative approaches to seismic data processing for the quantification of the appraisal of small, proven gas reservoirs in the Dutch North Sea. Over the last tens of years several gas prospects have been discovered in the North Sea. The Dutch part of the North Sea has been extensively mapped with 2D and 3D seismic datasets, which resulted in the discovery of many small and larger gas fields. However, especially for the smaller prospects it is not clear if these are economically viable based on the used seismic processing and imaging techniques. A drawback of the used seismic datasets is that their sampling and subsurface coverage is relatively sparse, making it difficult to extract reliable subsurface information. This means that the uncertainty of the quantification of reservoir potential is too high when it comes to business decisions.

Therefore, a case study of the presented tools was performed for a dataset in an area of interest within the Q1Q4 license block offshore the Netherlands in the Southern North Sea.

6.2. Full Wavefield migration of the pre-stack seismic surface data

As was demonstrated in Chapter 2, one of the challenges for reservoir characterisation is the strong reflecting properties in the overburden, yielding multiple reflection (i.e. noise) in the reservoir area, where reflectivity values are typically much lower. Despite the fact that internal multiples have a strength in the order of R^3 is R is the reflection strength in the overburden, it could be that this value is larger than the reflection of a reservoir layer.

Full Wavefield Migration has the promise of suppressing overburden multiples during the migration or redatuming process. For a synthetic dataset this was clearly demonstrated in Chapter 5, where strong overburden multiples hampered the seismic inversion process.

For this purpose we have selected the raw, pre-stack data with sources and receivers within a 10 x 10 km area around the intended well location (Q4-10). In this way we would be able to image an area at least as large as 5 x 5 km area. A schematic overview of the sources and receivers involved in the selected data is shown in Figure 6.1. Note that from the available data, only a relatively coarse subset of sources was used (the red dots), in total 350 for the total area.

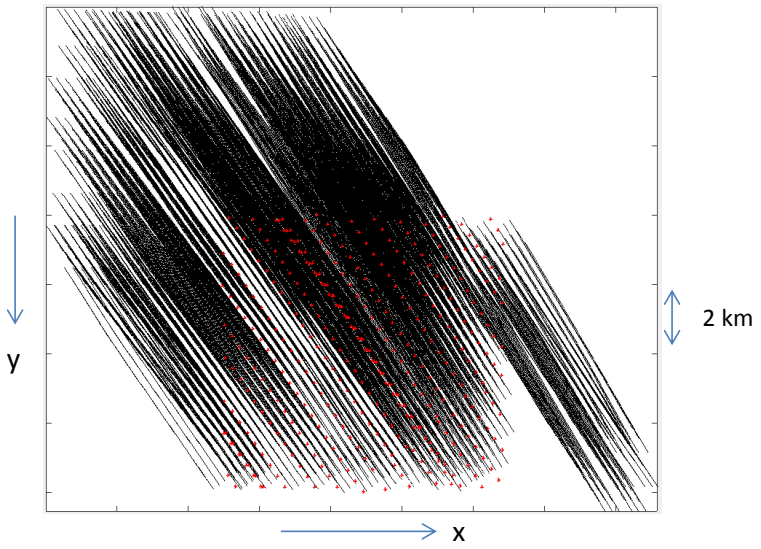

Figure 6.1: Graph of the data used for the 3D imaging with sources in red and receivers in black. b) Depth slice at z=2505, least-squares migration result. c) Depth slice at z=2505, Full Wavefield Migration result.

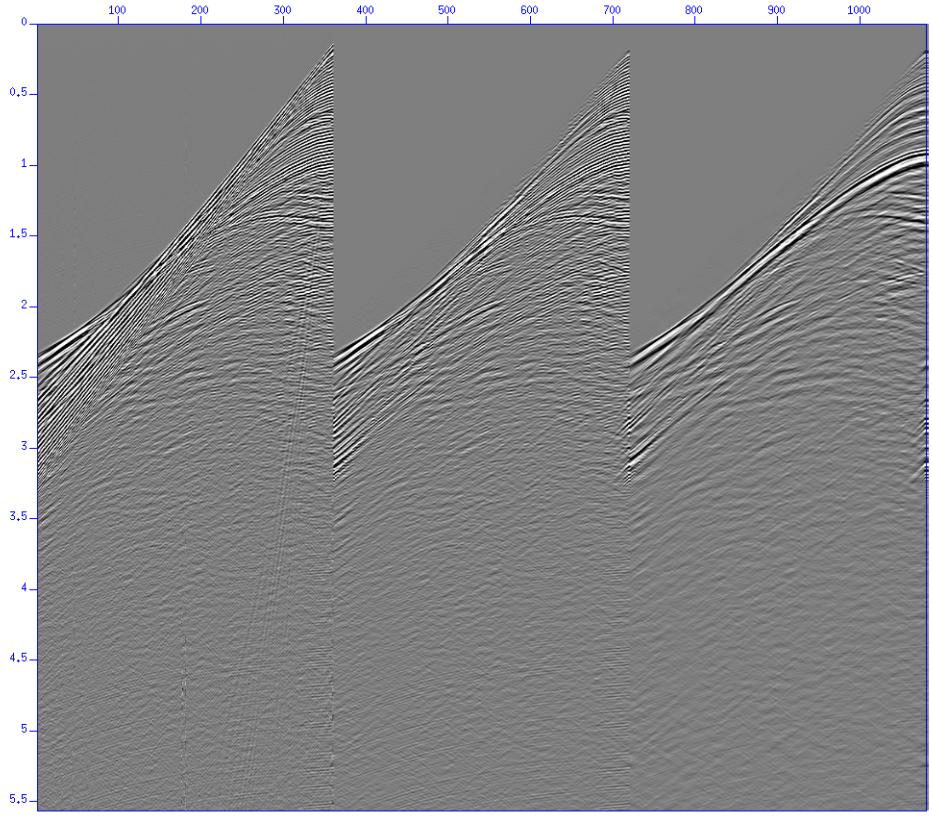

Figure 6.2: One selected shot record for one streamer from the 3d dataset. (left) Raw shot record, (middle) Shot after FK filtering. (right) Shot after additional predictive deconvolution.

6.2.1. Preprocessing

Figure 6.2, left panel, shows one shot record of the raw field data, after some band-pass filtering. Next, the data has been FK filtered to remove noise and also the steepest events that are not associated to the desired reflection information. The result for the shot record is shown in the middle panel of Figure 6.2.

Clearly, we can see in the two left panels in Figure 6.2 the short-period multiple reverberations, as a short period ringing effect, because the water depth in this region is only 30m. Although FWM can in theory handle all (surface) multiples, we do not expect extra illumination from these shallow water reverberations. They are merely copies of primary reflections that are recorded and will only make FWM more complicated, as all associated cross-talk has to be suppressed during the inversion iterations, while the added value is very minor. Therefore, we apply a predictive deconvolution in order to removal these reverberations and let FWM concentrate on other multiples in the data. The result of the predictive deconvolution is shown in the right panel of Figure 6.2. Note that now all subsurface reflections are clearly visible and the short period reverberations are successfully suppressed. These data are used as input for the FWM process.

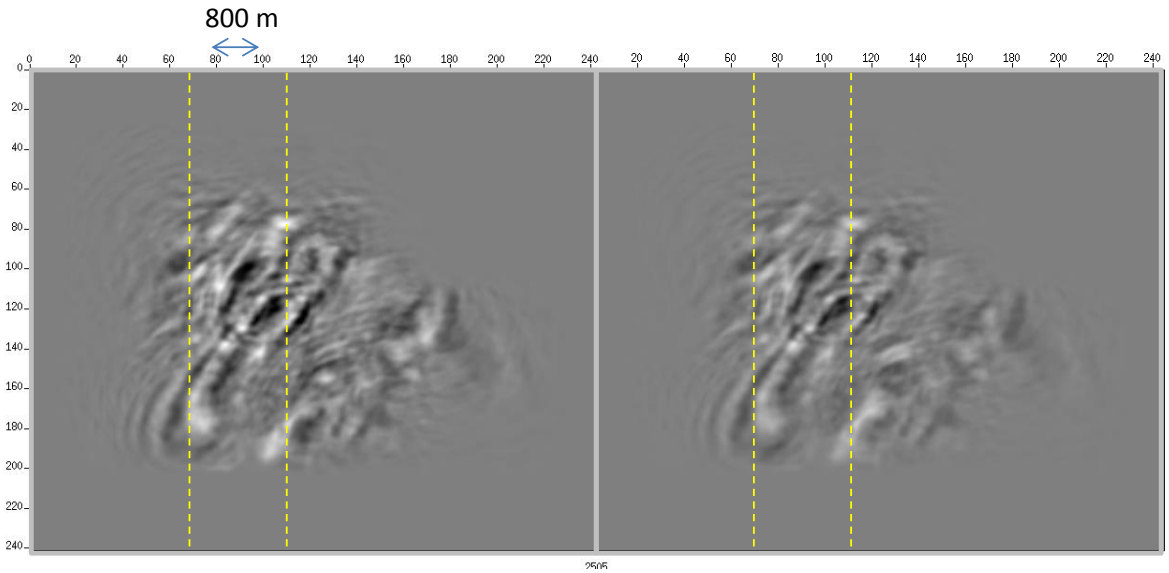

a) Depth slice, least-squares migration b) Depth slice, full wavefield migration

Figure 6.3: a) Depth slice at z=2505, least-squares migration result. b) Depth slice at z=2505, Full Wavefield Migration result.

6.2.2. Full Wavefield Migration

Next, the full wavefield migration process has been appied up to 30 Hz maximum frequency and on a 40 x 40 m spatial grid size (and 15m in depth). The FWM has bene run in two modes: by neglecting transmission effects and internal multiples - thus resembling least-squares migration - and in the full wavefield mode, where transmission effects and internal multiples are included. This means that in the FWM mode in the forward modeling from the current reflection image seismic reflection events

are (re)modeled including transmission from each reflection element and by including internal multiples modeled from the estimated relectivity image. So both aspects are included in a full data-driven manner, such that potential velocity erors will not influence (much) the generation of these scattering effects.

Figure 6.3 shows one depth slice from the image volume of the primaries-only option (a) and the FWM result (b). The lateral extend of the images can be linked to the acquisition geometry of the selected data, shown in Figure 6.1. The circles in Figures 6.3a (mostly on the left side) indicate internal multiples. Note that in the FWM results this imprint is reduced (although not fully suppressed).

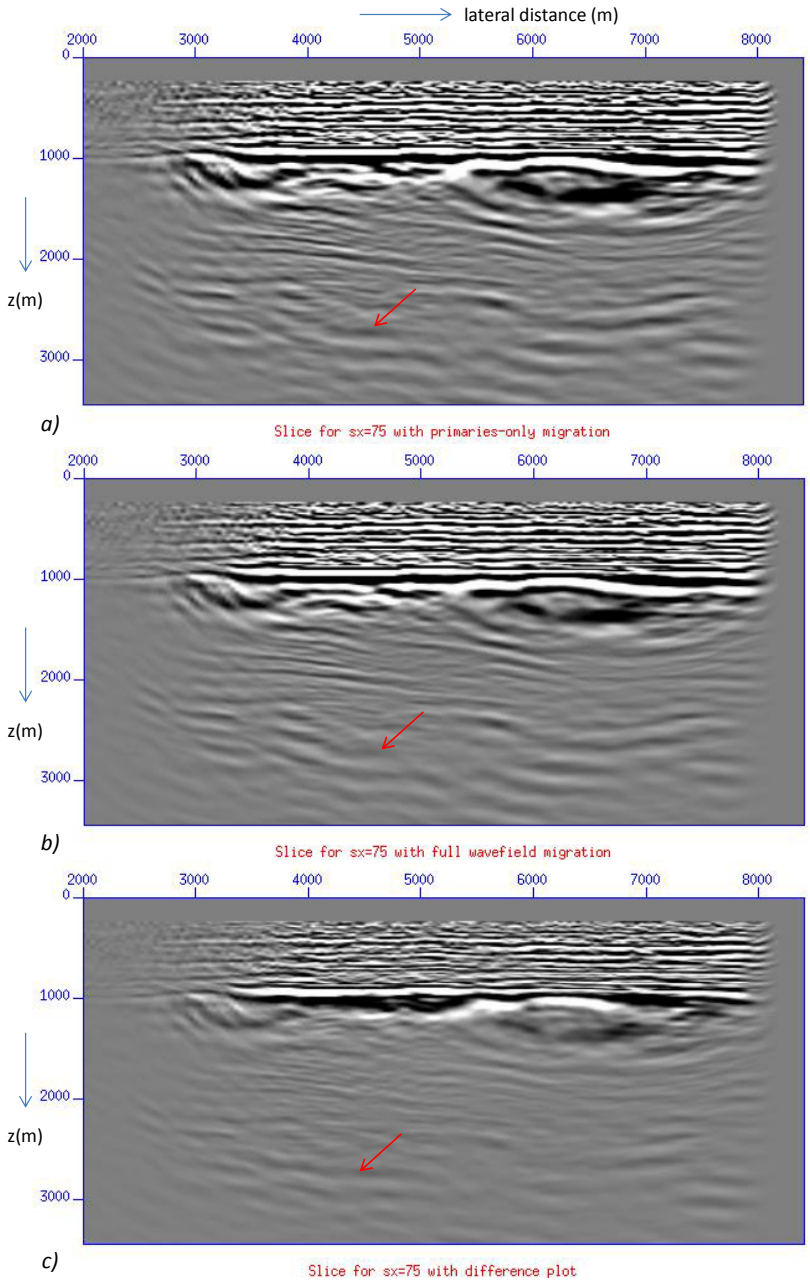

Figure 6.4: One slice of 3D image volume. a) Least-squares migration result. b) Full Wavefield Migration result. c) Difference.

Figures 6.4 and 6.5 show the imaging results for two slices along constant x-locations, for which the locations are indicated wit the yellow lines in Figure 6.3. Note that these slices are not selected along the sail direction but with a certain angle to the sail direction (along the Cartesian x-coordinate).

The main conclusions of this FWM field data study are:

- The use of surface multiples is less relevant in very shallow water scenarios.
- Strong internal multiples are present in the geology in the North Sea, however, the ability of FWM to fully suppress them needs more investigations

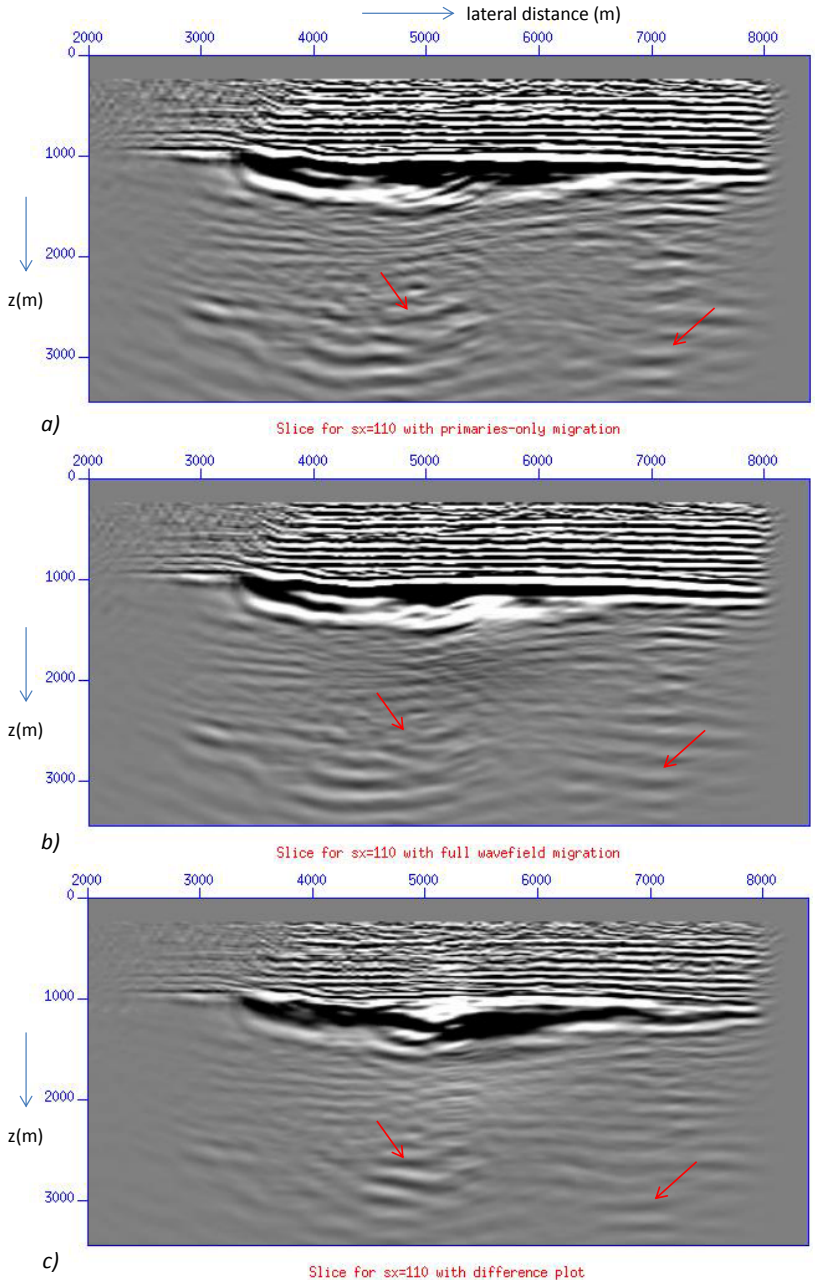

Figure 6.5: One slice of 3D image volume. a) Least-squares migration result. b) Full Wavefield Migration result. c) Difference.

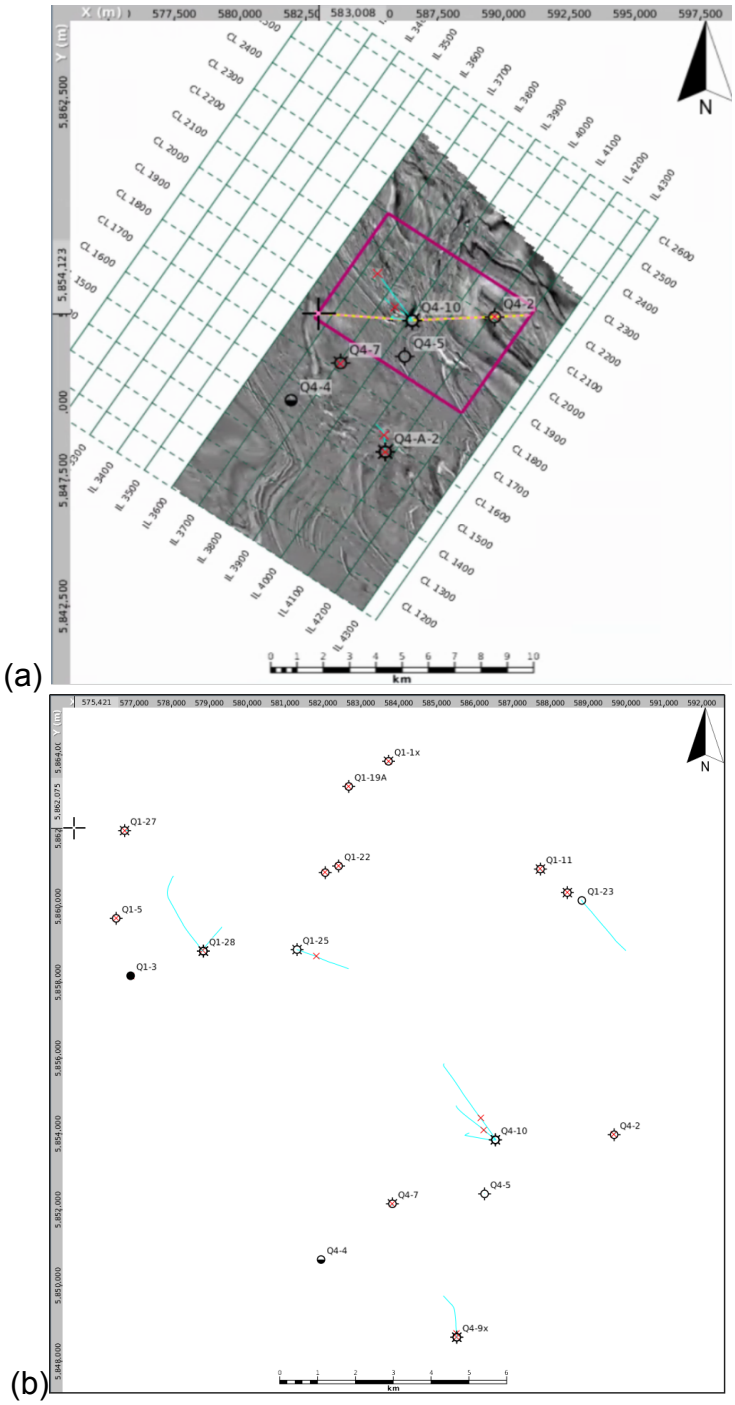

Figure 6.6: (top) Seismic coverage (horizontal slice) and AOI polygon for input to the 3D inversion (purple). (bottom) Map view of total well coverage (Q1 and Q4 area wells) as provided to Delft Inversion by Wintershall.

6.3. WEB-AVO on the migrated volumes

A Wave Equation Based (WEB) AVO inversion project was performed in an area of interest within the Q1Q4 license block offshore the Netherlands in the Southern North Sea. The objective of this project was to invert PSDM offset gathers for elastic properties that can provide information about spatial distribution of main gas reservoirs with this block, including a possible separation between live and residual gas. 6.6 shows the seismic coverage and the area of interest (AOI) for input to the 3D inversion as well as the available well data.
The AOI for the 3D inversion was selected based on the seismic data availability and centred around well (Q4-10), covering as well the Q4-C1, Q4-C2 and Q4-C3 sidetrack wells producing the Q1-B field. The surface coverage was estimated at 33.7 km2.

6.3.1. Scope of work

The work carried out can be summarised to:

- Initial data evaluation and analysis; Identify gaps in data availability/coverage and access if the currently available data are sufficient to curry out the 3D inversion work.
- Build low-frequency background models for the elastic properties (Ï□, Vp and Vs) extracted from wells in the AOI.
- Conversion of offset to slowness gathers over the target interval. The conversion is carried out via analytic ray-tracing in a stratified media and relies on the provided 3D velocity model.
- Seismic-to-well matching at well locations. This process yields the slowness dependent wavelets which are used in the inversion. The wavelets contain the overall calibration factor, as well as correction for the overburden transmission effects and can be interpolated over the entire AOI if more than one well are used in the analysis.
- Inversion of the seismic data at well locations and over the target area for the selected AOI on a 25 m x 25 m grid.
- Validation of the results.

6.3.2. Inversion results

An inversion of the total volume of data was performed over the area and window of interest. Figure 6.7 depicts the inversion results obtained at well Q4-2; a good match of elastic parameters is observed.

For illustration purposes, the input and results are displayed along a line that crosses a few wells of interest, see yellow line drawn on the left top view of Figure 6.6. Figure 6.8 shows the stack of the input seismic data along this line, whereas Figures 6.9 and 6.10 show the obtained compressibility and shear compliance volumes, respectively.

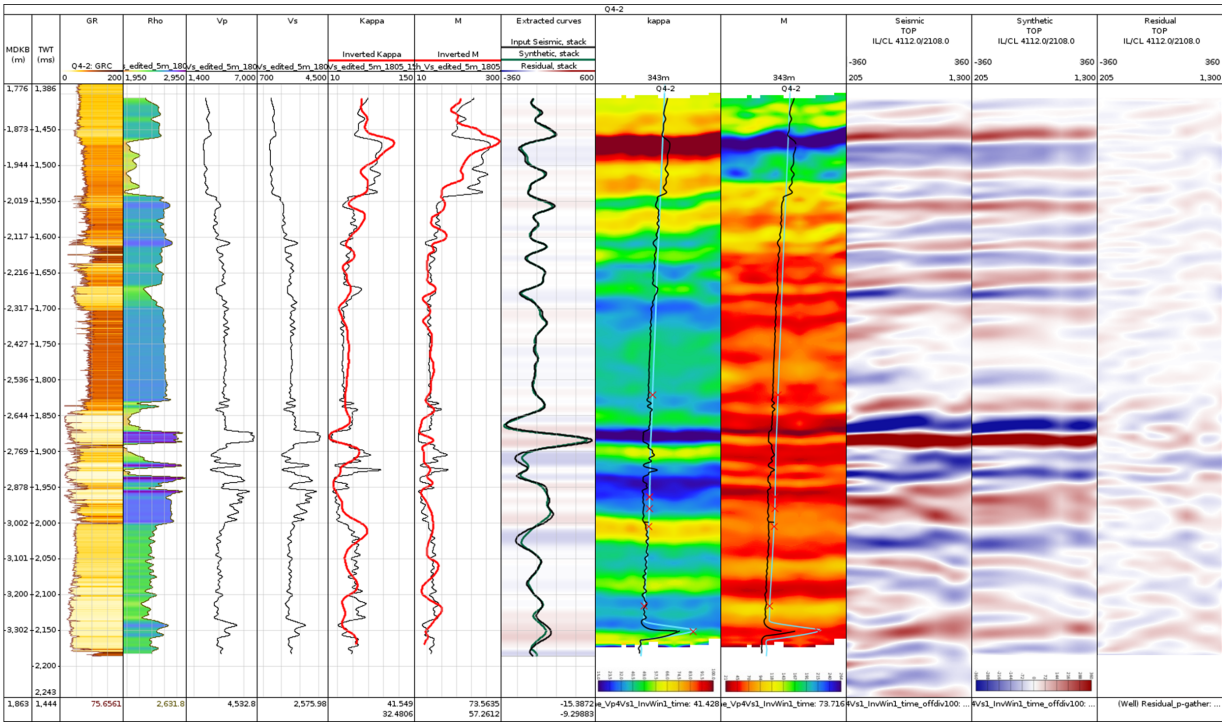

Figure 6.7: WEB-AVO Inversion results panel at well location Q4-2.

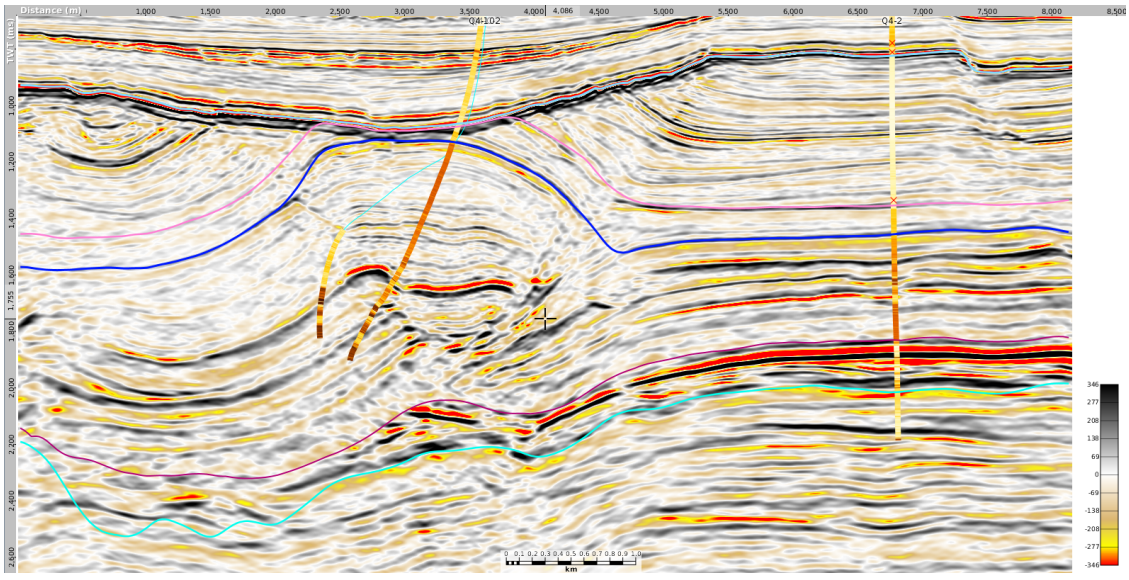

Figure 6.8: Full offset stack along the line. Displayed logs along well paths are gamma ray.

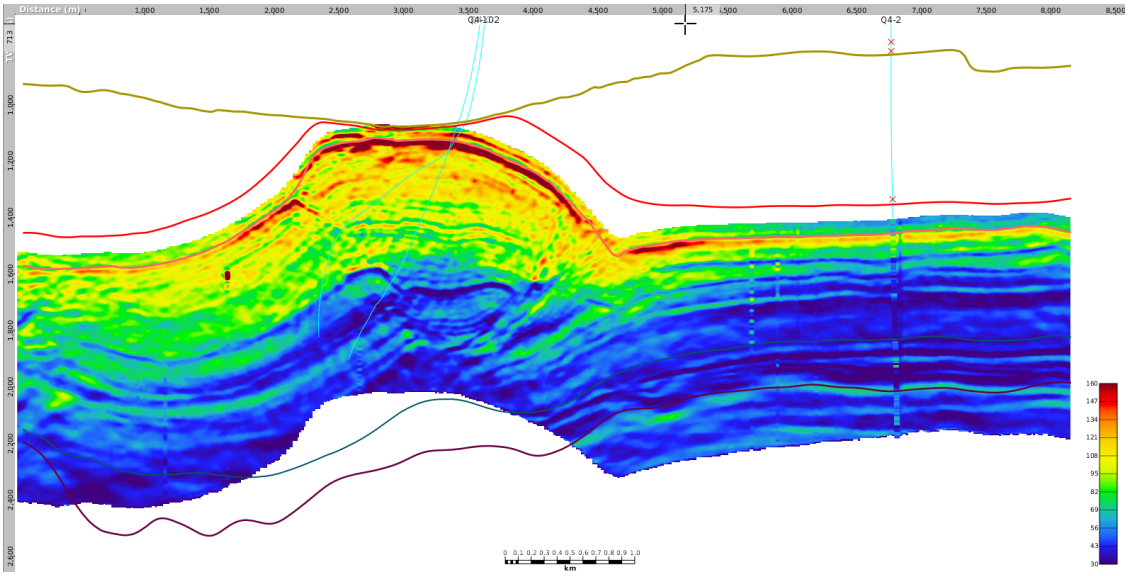

Figure 6.9: Compressibility along the line.

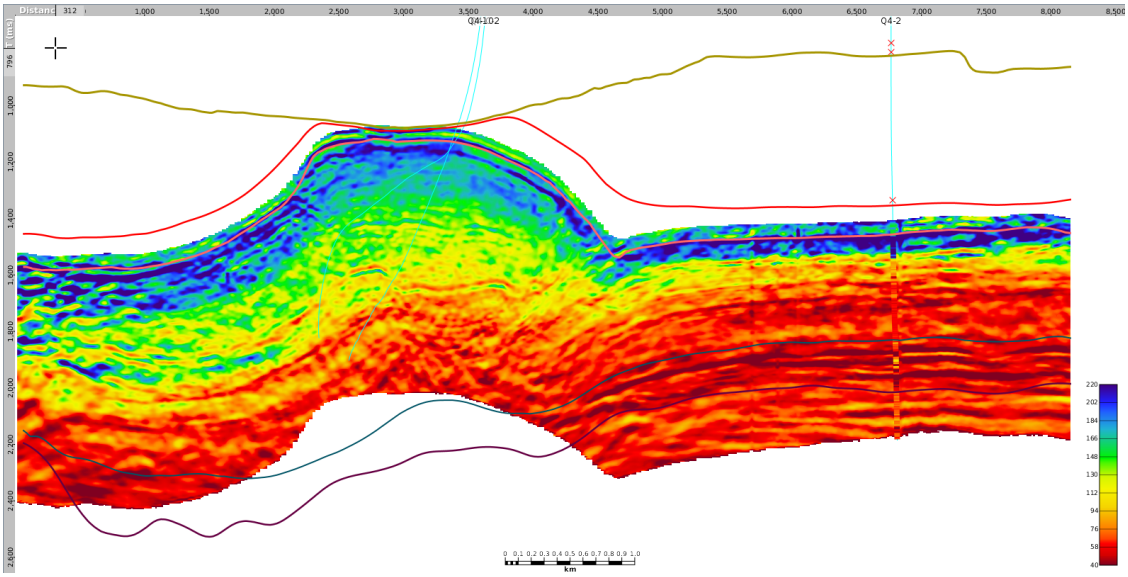

Figure 6.10: Shear Compliance along the line.

6.3.3. Concluding remarks on WEB-AVO inversion

The main conclusions of this WEB-AVO study were:

- The main challenges of this project are inherent in the underlying geology of the subsurface in the area of interest and the complex imaging problem it represents. The seismic data had been acquired using a narrow azimuth streamer with a rather limited offset to provide sufficient illumination to some particularly complex structures. A more accurate velocity model, guided by the FWI technology may help to resolve some of the issues present in the data for future reservoir characterization work but the re-processing work is still ongoing.
- Another challenge was sub-optimal well coverage and data availability, especially shear sonic logs which are important for the WEB AVO inversion approach. Vs velocity property was predicted, where possible, from available P-sonic, density and gamma-ray logs. It helped in making the background model more accurate and provided a basis for extracting a realistic wavelet at Q4-2 well location.
- Frequency content of input seismic was sufficient to achieve a satisfactory match to the well data at Q4-2 well location and extract a realistic wavelet for the inversion. Inversion of seismic data showed good match to compressibility computed from log properties. The inversion for shear compliance was not as reliable.
- Due to the complexity of the setting, further interpretation of the data needs to take place in order to derive the sensitivity of the produced cubes to saturation as well as to be used for prospectivity analysis.

7
WP5: Business Case

7.1. Introduction

This project has span 4 years, during which significant events have taken place in the Exploration and Production scene of the Netherlands. The decline of production of the Groningen gas field has sparked initiative -at the time of the compilation of the project proposal- that other sources of gas will be explored, such as the shallow gas fields offshore Netherlands. However, the continued low price of oil and gas has not been encouraging for further investments in the Dutch North Sea. Moreover, the transition to cleaner and renewable sources of energy has diverted a lot of investments to that field of activity. The impact of this transition on the objectives of the current project is large.

7.2. Market size

The technology developed during the VEGAS project was targeting the characterisation of -primarily- shallow gas accumulations, offshore the Netherlands, for exploration purposes. One robust way to measure the exploration activity over the last few years is by monitoring the number of exploration wells drilled. nlog.nl reports that in 2019, only 2 exploration and 7 development wells were drilled offshore the Netherlands (see 'Boringen beëindigd in 2019', nlog.nl), compared to 15 exploration and 31 development wells drilled in 2015, despite the collapse of oil prices in 2014. This supports the notion that investment has been diverting from the dutch exploration and production activity. In turn, this reduces the size of the Dutch seismic re-processing market as the need for such services is not yet required for this cause. Moreover, no shallow gas development project has been reported the last few years, despite the publicity attracted by EBN, see "The Netherlands Exploration Opportunities" brochure (authors, 2018).

However, this is hardly a phenomenon only expressed in the Netherlands. The chart of Figure 7.1 shows the decline in exploration activity of most of the hydrocarbon producing countries of Northern Europe.

7.3. Business case

The envisaged business case would have been based on robust technical results from the application of the developed work-flow on freely available data (from nlog.nl) in order to help de-risk the development of marginal or shallow gas fields offshore the Netherlands. Unfortunately, the business case has not proven to be strong mainly because:

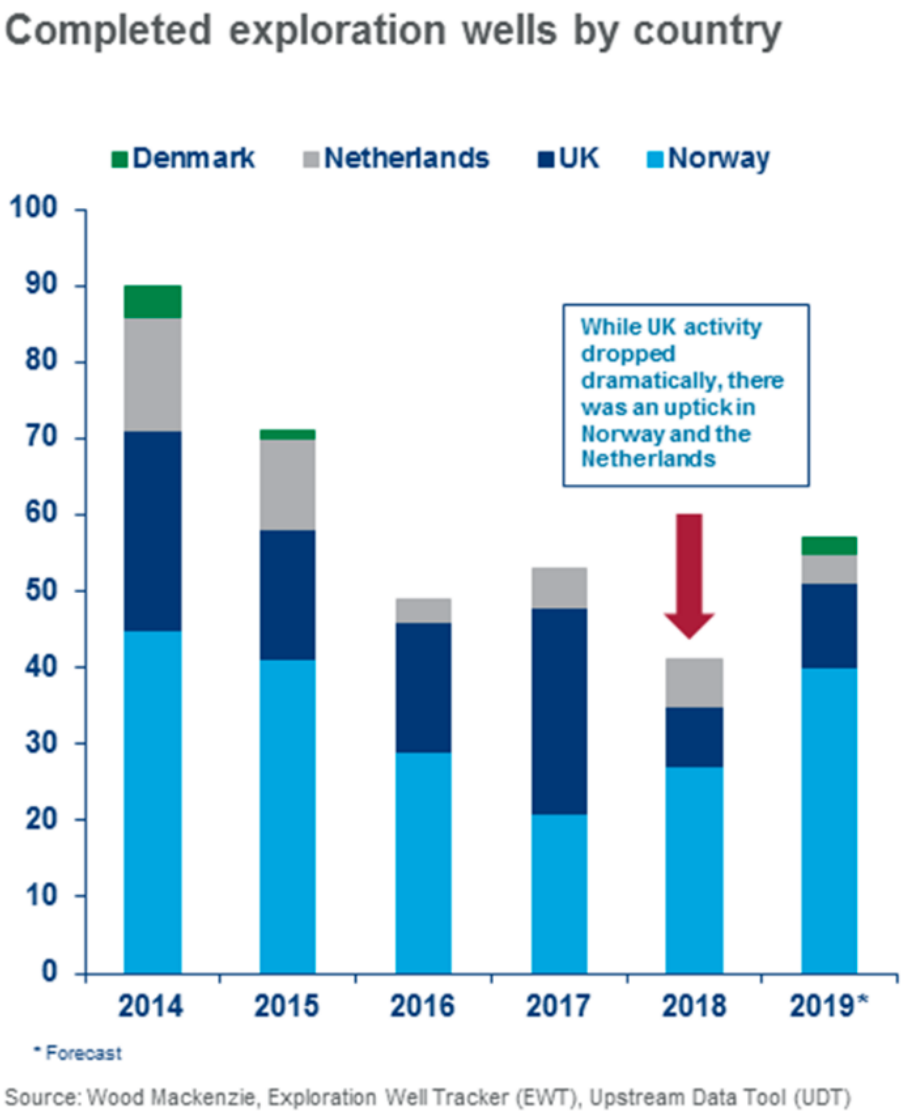

Figure 7.1: Exploration activity can be monitored by the number of exploration wells drilled every year. This chart clearly illustrates the overall decline in activity for northern European states, as well as the individual activity of the Netherlands.

- The interest in developing further gas fields has been limited as shown by the drilling activity above. This is due to non-technical reasons as investment has been diverted to other forms of energy.

- The technical feasibility was not successful in demonstrating a clear technological advantage of this work-flow, mainly due to the quality and lack of sufficient data, as illustrated in the previous chapters.

Another weakness of the proposed work-flow was that it focused primarily in a geophysical solution for the characterisation. Given the lack of data but the abundance of geological knowledge, a better focus in integrating different disciplines may have been more successful in demonstrating the added value of the work-flow, as it would

be able to directly measure, for instance, the value of information extracted in a reduction of the P10-P90 uncertainty range of a gas field. These lessons have been incorporated in further attempts to add value using the proposed algorithms in the realm of exploration for geothermal energy.

However, opportunities for further business development lie outside the Netherlands and Europe, in regions that face very specific problems that can be addressed by the proposed work-flow. Such regions are:

- Malaysia / Indonesia: Shallow gas accumulations represent a hazard rather than a target in these regions as these pockets throw a shadow over the deeper sections of interest. A work-flow that can perform imaging in such regions -as the one developed here- could have significant impact and success.
- Myanmar: Slumps deposited on the water bottom or right below obscure the seismic images below, creating ambiguity over the prospects and their size and fill.
- Brasil: The most prolific hydrocarbon region of Brazil consists of the pre-salt offshore basins, which need the combined work-flow developed here to be able to image the reservoir.

8 Conclusions

In this chapter the main conclusions of all parts of the project are summarised:

- Full wavefield imaging and redatuming approach
  It has been demonstrated on a synthetic 2D and 3D data (Chapters 2 and 5) that with he full wavefield redatuming approach a correction of overburden imprint on the reservoir response

- The WEB-AVO inversion process
  The synthetic data study showed that WEB-AVO is able to use the output of the 3D full wavefield redatuming approach and invert for the elastic parameters. The overburden imprint was removed by the full wavefield redatuming approach, which showed a clear uplift for the WEB-AVO output. The nonlinear inversion process embedded in WEB-AVO could further suppress the potential artifacts from the redatuming process.

- Field data application 3D full wavefield redatuming
  The North Sea field could not demonstrated all the virtues of the proposed 3D seismic tool. Especially the full wavefield redatuming process could not benefit from the surface multiples, because of the very shallow water layer. FWM has been used in deeper water with success, but the small water depth (30m) limits the use of exploiting the multiples.
  For the internal multiples generated in the salt region some first hints of multiple reduction can be observed, however, a complete suppression could not be yet achieved.
  Some more research need be done in the optimum imaging of the 3D streamer-type data, where the re-injection of seismic data from the surface need be done in a full 3D sense, and not only from the seismic cable locations. So the method needs to be accompanied by a prior interpolation of the streamer data in order to create a consistent physical relationship between downging and upgoing (measured) wavefields.

- Field data application WEB-AVO
  The WEB-AVO could successfully be applied on the migrated sections that were made available by the Wintershall and provided inversion results for the compressibility κ and shear compliance M.
  Frequency content below the salt were good enough, although the method was probably hampered by limited illumination from the narrow azimuth streamer geometry and possible migration-velocity errors – in combination with the complex geological sub-salt setting – to provided more accurate focusing of the data.

Acknowledgements

This public report is related to Project TEUG116268 that has been executed with a grant from the Ministry of Economic affairs ('Topsector Energiesubsidie van het Ministerie van Economische Zaken')

Wintershall Noordzee B.V. is acknowledged for providing the prestack field data for the North Sea as well as the migrated volume for the reservoir inversion and all auxiliary information required to finalize the field data examples. Especially Marc Beller and Andires Wever from Wintershall Noordzee B.V. are thanked for their support and help.

Bibliography

Arabie, P., Hubert, L. J., and Soete, G. D., 1996, Clustering and classification: World Scientific Publishing. ISBN: 981-02-1287-9.

authors, V., 2018, The Netherlands Exploration opportunities, ebn and tno and ministry of economic affairs & climate policy: https://www.ebn.nl/wp-content/uploads/2019/02/ReducedExploratie-brochure-EBN.pdf; retrieved 30 May 2020.

Berkhout, A. J., 1982, Seismic migration, imaging of acoustic energy by wave field extrapolation, A: theoretical aspects: Elsevier (second edition).

Berkhout, A. J., 2014a, Review paper: An outlook on the future of seismic imaging, part I: forward and reverse modelling: Geophysical Prospecting, **62**, no. 5, 911–930.

——— 2014b, Review paper: An outlook on the future of seismic imaging, part II: Full-wavefield migration: Geophysical Prospecting, **62**, no. 5, 931–949.

Berryhill, J. R., 1984, Wave equation datuming before stack (short note): Geophysics, **49**, no. 11, 2064–2066.

Davydenko, M., and Verschuur, D., 2017, Full-wavefield migration: using surface and internal multiples in imaging: Geophysical Prospecting, **65**, no. 1, 7–21.

Garg, A., and Verschuur, D., 2016, Reservoir impulse response estimation using joint migration inversion: 78th EAGE Conference and Exhibition 2016.

Gisolf, A., and van den Berg, P., 2012, Target-oriented elastic full wave form inversion: 74th EAGE Conference and Exhibition incorporating EUROPEC 2012.

Gisolf, A., in't Veld, R. H., Haffinger, P., Hanitzsch, C., Doulgeris, P., and Veeken, P. C. H., 2014, Non-linear full wavefield inversion applied to carboniferous reservoirs in the Wingate gas field: 76th EAGE Conference and Exhibition, EAGE, extended abstract.

Gisolf, A., Haffinger, P., and Doulgeris, P., 2015, Redatuming directly to angle gathers, for the purpose of target oriented quantitative interpretation: 77th EAGE Conference and Exhibition 2015.

Hinkley, D. ., Bear, G. W., and Dawson, C., 2004, Prestack gather flattening for AVO: 74th Ann. Internat. Mtg., Soc. Expl. Geophys., Expanded abstracts, 271–273.

Nocedal, J., and Wright, S. J., 2006, Numerical optimization: Springer Series in Operations Research and Financial Engineering. Springer, 2 edn.

Phillips, M., 2017, Automatic gather flattening for AVO analysis using amplitude-adjusted plane-wave destruction filters: 87th Ann. Internat. Mtg., Soc. Expl. Geophys., Expanded abstracts, 477–482.

Rizzuti, G., and Gisolf, A., 2017, An iterative method for 2D inverse scattering problems by alternating reconstruction of medium properties and wavefields: theory and application to the inversion of elastic waveforms: Inverse Problems, **33**, no. 3, 035003.

Russell, S., and Norvig, P., 1995, Artificial Intelligence: A modern approach): Prentice Hall. ISBN 978-0137903955.

Sigismondi, M., 2017, The impact of near traces conditioning on prestack characterization: 87th Ann. Internat. Mtg., Soc. Expl. Geophys., Expanded abstracts, 718–722.

Silva, R., Baroni, L., Ferreira, R., Salles Civitarese, D., Szwarcman, D., and Vital Brazil, E., 03 2019, Netherlands dataset: A new public dataset for machine learning in seismic interpretation: arXiv,org, Compter Science, Machine Learning.

van Winden, M., 2015, Salt tectonics in the northern dutch offshore - a study into zechstein halokinesis in the dutch central graben and step graben: Masters's thesis, Utrecht University.

Wapenaar, C. P. A., and Berkhout, A. J., 1989, Elastic wave field extrapolation: redatuming of single- and multi-component seismic data: Elsevier Science Publ. Co., Inc.